

Multivariate Regression Analysis of Gravitational Waves from Rotating Core Collapse

William J. Engels,^{1,*} Raymond Frey,^{1,†} and Christian D. Ott²

¹*Department of Physics, University of Oregon, Eugene, OR, USA*

²*TAPIR, California Institute of Technology, Pasadena, CA, USA*

Kavli Institute for the Physics and Mathematics of the Universe (Kavli IPMU; WPI), Kashiwa, Japan[‡]

(Dated: June 26, 2018)

We present a new multivariate regression model for analysis and parameter estimation of gravitational waves observed from well but not perfectly modeled sources such as core-collapse supernovae. Our approach is based on a principal component decomposition of simulated waveform catalogs. Instead of reconstructing waveforms by direct linear combination of physically meaningless principal components, we solve via least squares for the relationship that encodes the connection between chosen physical parameters and the principal component basis. Although our approach is linear, the waveforms' parameter dependence may be non-linear. For the case of gravitational waves from rotating core collapse, we show, using statistical hypothesis testing, that our method is capable of identifying the most important physical parameters that govern waveform morphology in the presence of simulated detector noise. We also demonstrate our method's ability to predict waveforms from a principal component basis given a set of physical progenitor parameters.

I. INTRODUCTION

Unimpeded by intervening material, gravitational waves (GWs) trace out bulk motions of matter in the sudden collapse of a dying massive star's core [1]. Hidden beneath the stellar envelope, these dynamics are inaccessible by traditional observational methods. After the star's iron core exceeds its effective Chandrasekhar mass, it grows gravitationally unstable and collapse ensues. The stiffening of the nuclear equation of state (EOS) at nuclear density leads to the rebound of the inner core ("core bounce") into the still infalling outer core, creating an outwardly propagating shock wave. According to simulations and basic theory (e.g., [2]), this shock wave quickly deteriorates and is not sufficiently energetic enough to expel the stellar material and drive a supernova explosion. Instead, it stalls and turns into an accretion shock. The yet uncertain *supernova mechanism* must revive the stalled shock. All currently discussed candidate mechanisms involve multi-dimensional bulk motions of matter in the region behind the stalled shock (e.g., [3]). Hence, the detection, analysis, and characterization of gravitational waves (GW) from core-collapse supernovae could potentially provide great insights into the uncertain mechanism that reignites the explosion.

As supernova theorists converge on accurate models to describe and predict the transition from core collapse to supernova explosion, advanced GW detectors such as Advanced LIGO [4] and Advanced Virgo [5] will begin taking data with \sim ten times greater sensitivity than their initial versions. Since the expected rate of galactic core-collapse supernovae is only $\sim 1 - 3$ per century (e.g., [6]), it is imperative to develop methods able to extract

as much information as possible from the GWs that will be observed from these rare events.

Theory and multi-dimensional simulations have identified a variety of GW emission processes, including rotating core collapse, nonaxisymmetric rotational instabilities, turbulent convection in the protoneutron star and in the region immediately behind the stalled shock, pulsations of the protoneutron star, and asymmetric outflows of mass-energy (see, e.g., [1, 7] for reviews). Of these emission processes, rotating core collapse is the most extensively studied and has received the most attention from GW data analysts.

In previous work, Brady and Majumdar [8] introduced a Gram-Schmidt method to parameterize rotating core collapse GW signals in terms of small numbers of orthonormal basis vectors encapsulating robust signal features extracted from a catalog of simulated waveforms by [9]. Heng [10] applied Principal Component Analysis (PCA) for the same purpose, and showed that the PC basis (PCs; principal components) provides a more efficient representation of waveform catalogs than Gram-Schmidt.

Summerscales *et al.* [11] studied the reconstruction of rotating core collapse waveforms of [12] injected into detector noise using a maximum entropy approach. They used cross-correlation of the reconstructed signal with catalog waveforms to determine parameters of the source.

Röver *et al.* [13] combined the PC basis approach of [10] with Bayesian inference (via Markov Chain Monte Carlo) to recover the linear combination of PC basis vectors that most accurately reconstructs a rotating core collapse GW signal buried in noise. They then compared the recovered linear combination coefficients to the coefficients associated with the rest of the catalog signals to infer the physical parameters of the detected signal in a nearest-neighbor-type scheme [14]. While able to produce excellent reconstructions, they had limited success inferring the physical parameters of the recovered waveform.

Different explosion mechanisms may have distinct and

* wengels@uoregon.edu

† rayfrey@uoregon.edu

‡ cott@tapir.caltech.edu

characteristic GW signatures [1, 15]. Exploiting this possibility, Logue *et al.* [16] developed a Bayesian model selection framework with the aim of inferring the explosion mechanism on the basis of a GW signal in the presence of detector noise. They used PC-decomposed waveform catalogs from simulations addressing various GW emission models and computed the Bayesian evidence to infer which catalog best reconstructs an injected signal.

The above previous work has demonstrated that PCA is a powerful tool to extract robust features from an ensemble of waveforms modeling different realizations (random realizations and/or variations of model parameters) of the same GW emission process. However, as already noted by [10, 13, 16], PCA’s major disadvantage is that the PCs do not directly encode the *physical parameters* of the simulated collapse models whose GW waveforms they represent. This is a major limitation to their application in Bayesian inference beyond model selection.

In this paper, we present a multivariate regression approach that expresses the set of waveforms in a given core-collapse supernova GW catalog as a linear combination of vectors, each corresponding to features *directly* attributable to progenitor characteristics. Each of these waveform feature vectors is subsequently expressed as a linear combination of PCs, providing a bridge between physical parameters and PCs that is missing in previous work. This method of decomposing a waveform catalog allows us to characterize linear and non-linear relationships between waveforms and physical parameters.

A similar multivariate regression approach was first used by Potthoff and Roy [17] to conduct an analysis of variance of growth curves. Instead of a PC basis, they used a polynomial basis to study the influence of different treatments on the growth of animal subjects over time. Zerbe and Jones [18] used a Fourier basis to analyze circadian rhythm data. Using the rotating core collapse waveform catalog of Abdikamalov *et al.* [19], we show that the statistical significance of these relationships can be assessed via standard test statistics. By operating in the Fourier domain, we can straightforwardly take corrupting detector noise into account in these tests.

While we concentrate on applying our approach in an analysis of the relationships between physical parameters and waveform features for rotating core collapse, we also demonstrate that the method presented can be used to construct rotating core collapse gravitational waveform predictions using physical parameters as input. This work thus paves the way for a template-bank based parameter estimation approach for gravitational waves from rotating core collapse.

This paper is structured as follows. In Sec. II, we introduce the motivating rotating core collapse waveform catalog and develop a statistical model for its analysis. In Sec. II A, we review the physical parameter space used in the Abdikamalov *et al.* waveform catalog. In Secs. II B and II C, we detail the steps we take to mathematically describe a linear relationship between the gravitational waveforms, features associated with physical parameters

and additive detector noise. Sections II D and II E elaborate on how physical parameters are encoded into our statistical model and our use of the SVD basis to construct feature vectors. In Sec. II F, we provide least squares solutions which estimate the feature vectors and their covariances. In Secs. II G through Sec. III C, we present an analysis of the relationships between physical parameters and the waveforms of the Abdikamalov *et al.* core-collapse waveform catalog. Finally in Sec. III D, we use our multivariate model to construct waveforms not previously included in the analysis, and then compare our predictions to the actual waveforms simulated by Abdikamalov *et al.* in Sec. III E.

II. METHODS AND INPUTS

A. The Abdikamalov *et al.* Waveform Catalog

Rapid rotation, in combination with strong magnetic fields, has been suggested to enable a *magnetorotational mechanism* for core-collapse supernova explosions (e.g., [20, 21]). In this mechanism, angular momentum conservation leads to a rapidly differentially spinning post-bounce core. The magnetorotational instability (MRI; e.g., [22]) is invoked to extract differential rotation energy and produce a local magnetar-strength magnetic field. Depending on the initial rotation rate (which should be fast enough to make a millisecond-period protoneutron star) and the presence of a dynamo process that converts local unordered field into global field, toroidal field strength of up to $10^{15} - 10^{16}$ G may be obtained. If this is indeed the case, a number of axisymmetric (2D) simulations have shown that strong bipolar jet-like outflows develop that drive an explosion (e.g., [20, 21, 23]). Recent full 3D simulations reported in [24] suggest that in 3D the jet is distorted by nonaxisymmetric instabilities and if an outflow develops, it will not be as neatly collimated as in the 2D case.

A rapidly rotating core has a natural quadrupole moment due to its flattening by the centrifugal force. The extreme accelerations at core bounce lead to a rapid and large-scale change in the quadrupole moment. This gives rise to a characteristic GW signal that is predominantly linearly polarized (e.g., [25, 26]). This signal is so distinct from other GW emission processes in core-collapse supernovae that it is possible to use it as an indicator for the rapid rotation required for magnetorotational explosions [1, 15, 16].

Abdikamalov *et al.* [19] recently carried out 135 axisymmetric general-relativistic hydrodynamic simulations of rotating core collapse¹. Since the GW signal from rotating core collapse is essentially independent of

¹ The Abdikamalov *et al.* waveform catalog is available at <http://stellarcollapse.org/ccdiffrot>.

progenitor star mass [27], they performed their simulations starting with the core of a presupernova star that had a mass of $12 M_{\odot}$ at zero-age main sequence.

Abdikamalov *et al.* systematically varied the initial central angular velocity Ω_c from 1 rad s^{-1} to 15.5 rad s^{-1} and considered five different length scales for differential rotation of $A1 = 300 \text{ km}$, $A2 = 417 \text{ km}$, $A3 = 634 \text{ km}$, $A4 = 1268 \text{ km}$, and $A5 = 10000 \text{ km}$ (see their Eq. 1). The Abdikamalov *et al.* waveforms are split into a set of 92 “catalog” waveforms and a set of 43 “injection” waveforms. The injection waveforms have one of the A values listed in the above, but values of Ω_c in between those covered by the catalog waveforms. A small set of injection waveforms was calculated with a different equation of state and with variations in the electron capture prescription during collapse. Abdikamalov *et al.* used the injection waveforms to test their algorithms for extracting total rotation and precollapse differential rotation from an observed signal. In the present study, we primarily use the 92 catalog waveforms and at times the subset of the injection waveforms that does not include waveforms computed with different equation of state and electron capture prescription. Figure 1 shows a superposition of all 92 catalog waveforms (aligned to the time of core bounce) and the mean waveform obtained by computing the average over all waveforms.

While Abdikamalov *et al.* set up their models in the above way, they point out that the initial angular velocity Ω_c is not a good parameter to study: Progenitor cores with different structure (e.g., less or more compact), but with the same Ω_c will lead to different rotation rates at bounce, since, due to angular momentum conservation, Ω increases $\propto r^{-2}$. So an initially further-out mass element (at greater initial r) will spin up more than an initially further-in mass element at the same initial Ω_c . Abdikamalov *et al.* find that both the angular momentum content of the inner core *measured at bounce* and its ratio of rotational kinetic energy to gravitational energy $\beta_{\text{ic,b}} = (T/|W|)_{\text{ic,b}}$ are much more robust parameters and are approximately independent of progenitor structure [27]. We note that the degree of precollapse differential rotation is subject to very similar degeneracies as the precollapse Ω_c . A given fixed value of A will lead to different inner core rotation at bounce for different progenitor structure, even if the total angular momentum inside the inner core is the same. Hence, the results on differential rotation obtained by Abdikamalov *et al.* are progenitor dependent (the strength of this dependency remains to be established) and so will be the results on differential rotation presented in this paper.

Another limitation of the Abdikamalov *et al.* study is the use of only five discrete values of the differential rotation parameter A , which is rather sparse and may not fully probe the range of effects that variations in differential rotation may have on rotating core collapse waveforms.

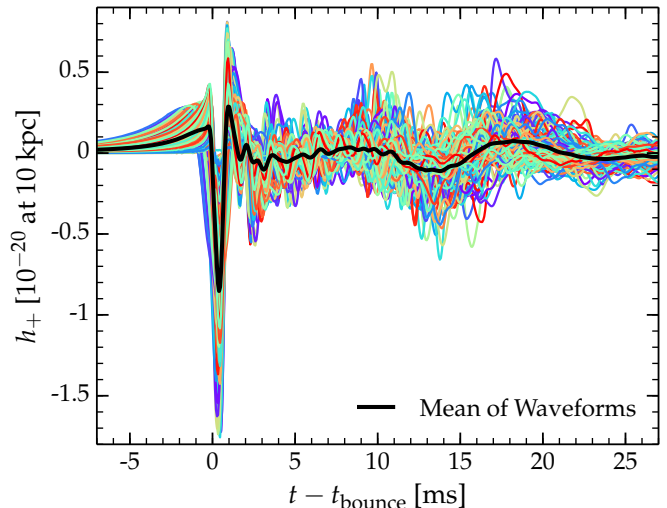


FIG. 1. The 92 GW waveforms from the primary Abdikamalov *et al.* catalog superimposed in varying colors. The waveforms are aligned to the point in time of core bounce and are resampled to have the same sampling frequency. The mean waveform of the catalog is overlaid in black. It is computed by taking the mean of the 92 waveforms at each point in time.

B. Multivariate Regression Model: Overview

In the following sections, we describe in detail the methodology required to construct a multivariate regression model for GWs from rotating core collapse. First, in II C, we construct the baseline statistical model step by step. In the resulting matrix equation, the Fourier domain GW catalog waveforms are simultaneously expressed as linear combinations of a yet unknown set of feature vectors. Each feature vector signifies an effect contributed to the rotating core collapse GW signals associated with a physical parameter. In Sec. II D, we describe useful methods to encode representations of the physical parameters of the progenitors into our statistical model. Then in Sec. II E, we express the feature vectors that characterize initial parameter effects themselves as linear combinations of PCs, a set of orthonormal basis vectors. This basis is derived using Singular Value Decomposition (SVD) [10, 28]. The resulting statistical model is given in Eq. 11. Finally, we provide the least squares solutions in II F and discuss the use of statistical hypothesis testing in Sec. II G.

C. Constructing the Statistical Model

We begin by describing the preprocessing of the time domain GWs, and then cast the statistical model in the frequency domain. In the time domain, each waveform in the catalog is interpolated to have a sampling frequency of 16384 Hz, Tukey windowed, and zero-padded. Then they are aligned to core bounce, which is determined by

the point in time where the core has the highest central density. The aligned waveforms are depicted in Fig. 1. The zero-padded ends of the waveforms are then truncated so each is one second long. Each waveform is then Fourier transformed, and the real and imaginary parts are kept unaltered. In order to obtain a set of principal component vectors (PCs), SVD is performed on the complex valued waveform catalog [10, 28]. The role this basis plays in the model is described in Sec. II E. For the detector noise model, we use the expected design-sensitivity zero-detuning high-power Advanced LIGO noise [29].

We describe the construction of the model in steps. First we construct a univariate version that considers just the i th waveform in the catalog, a $1 \times t$ vector \mathbf{y}_i , and its set of p physical parameters, the $1 \times p$ vector \mathbf{x}_i . We then expand the univariate equation into a full multivariate model, considering all waveforms in the catalog simultaneously. We describe how physical parameters are encoded into each vector \mathbf{x}_i in the univariate case and in the *design matrix* \mathbf{X} , in the multivariate case in Sec. II D.

The i th waveform in the catalog is written as a linear combination of unknown vectors arranged row-wise in \mathbf{M} ,

$$\mathbf{y}_i = \mathbf{x}_i \mathbf{M} + \mathbf{r}_i, \quad (1)$$

where \mathbf{M} is a $p \times t$ matrix of p unknown *feature vectors*. Each row vector, or feature vector, in \mathbf{M} represents the linear effect of a parameter value encoded in a column of the $1 \times p$ vector \mathbf{x} . We note that our use of term “feature vector” is semantically different than its use in the machine learning literature. In Sec. II E, we will return to \mathbf{M} and discuss it in more detail. The vectors \mathbf{y}_i and \mathbf{x}_i are known and represent the i th waveform and the i th set of initial conditions representing it, respectively.

Since some set of p feature vectors in \mathbf{M} is unlikely to provide a perfect linear reconstruction of \mathbf{y}_i , we include the vector \mathbf{r}_i as a residual error term. This residual is due only to the difference between the waveform \mathbf{y}_i and its linear model, $\mathbf{x}_i \mathbf{M}$. If \mathbf{M} could perfectly reconstruct all catalog waveforms then that would mean that our linear model and parameter encoding scheme was an exact predictor of waveform morphology for all catalog waveforms. Since core collapse is a highly complicated process, we describe model uncertainty by assuming that this residual is a complex multivariate normally distributed random vector [30] with zero mean and a covariance matrix denoted by Σ_R ,

$$\mathbf{r}_i \sim \mathcal{N}^C(\mathbf{0}, \Sigma_R). \quad (2)$$

We succinctly denote its multivariate normal probability distribution using sampling notation [31]. $\mathbf{v} \sim \mathcal{N}^C(\mathbf{a}, \Sigma)$ signifies a complex multivariate normally distributed random vector \mathbf{v} that is parameterized by its central location, or expectation value, $\mathbb{E}(\mathbf{v}) = \mathbf{a}$ and a positive-semidefinite covariance matrix Σ [32]. Note that we assume throughout that the real and complex parts of our complex normal random vectors are independent

(see Appendices of [13, 33]). The (i, j) element of a covariance matrix is defined as the covariance between the i and j elements of the random vector \mathbf{v} . Equivalently, we can write,

$$\Sigma_{i,j} = \mathbb{E}[(v_i - \mathbb{E}(v_i))(v_j - \mathbb{E}(v_j))^{\dagger}]. \quad (3)$$

When helpful, we will underset the dimensions of quantities written in matrix equations or written in sampling notation (where the \sim is read as “is sampled from”). Throughout this paper, we denote the conjugate transpose with \dagger , and a transpose of a real valued matrix with a superscript T .

Each element of the diagonal of Σ_R in Eq. 2 is then the covariance of the corresponding element of the vector \mathbf{r}_i with itself (the variance), and each off-diagonal element is the covariance between the i th and j th elements of \mathbf{r}_i . Assuming normality in the residuals is supported by the central limit theorem: sums or products of random variables tend towards a Gaussian distribution [30], and a Gaussian distributed random vector (time domain signal) implies gaussianity of its Fourier Transform [13]. If the normality assumption is applicable, the mean vector and covariance matrix completely characterize the random behavior of the system.

A model with increased uncertainty in the waveform due to GW detector noise is of much greater interest. We define $\mathbf{y}'_i \equiv \mathbf{y}_i + \mathbf{s}_i$, where \mathbf{s}_i is commonly approximated as a sample of additive, stationary, and colored Gaussian noise from a given GW detector. In the Fourier domain, the detector noise is commonly assumed to be of Gaussian character with zero mean and covariance matrix Σ_S ,

$$\mathbf{s}_i \sim \mathcal{N}^C(\mathbf{0}, \Sigma_S). \quad (4)$$

As commonly done in the GW data analysis community, we approximate Σ_S as the zero matrix, but set its diagonal elements to the variances of each frequency bin of the power spectral density (PSD) that characterizes the noise of a given detector [33, 34]. No approximation need be made however, and a full noise covariance matrix for a given detector could be used.

This allows us to rewrite Eq. 1 as,

$$\mathbf{y}'_i = \mathbf{x}_i \mathbf{M} + \mathbf{r}_i + \mathbf{s}_i. \quad (5)$$

Since the sum of two normally distributed random variables is also normally distributed [30, 31], we can combine the noise and error terms, setting $\mathbf{e}_i = \mathbf{s}_i + \mathbf{r}_i$. Equation 5 then becomes,

$$\mathbf{y}'_i = \mathbf{x}_i \mathbf{M} + \mathbf{e}_i, \quad (6a)$$

$$\mathbf{e}_i \sim \mathcal{N}^C(\mathbf{0}, \Sigma_R + \Sigma_S). \quad (6b)$$

From Eq. 5, we can see that the distance of the source (which sets the signal amplitude at the detector) determines the degree to which instances of additive detector

noise \mathbf{s}_i degrade the signals. Therefore, at the start of an analysis based on this model, each \mathbf{y}_i needs to be scaled to a given source distance.

Up until this point, the structure of our statistical model is identical to the model by Röver *et al.* [13]. Specifically, our Eq. 6a is essentially identical to their Eq. 6. However, we consider the feature vectors in \mathbf{M} to be unknown quantities, and each \mathbf{x}_i known beforehand. Past this point, we depart from the methodology of [13].

We form the multivariate analog of Eq. 6a by including all n waveforms \mathbf{y}_i and all n vectors \mathbf{x}_i into a matrix equation. Each \mathbf{y}'_i becomes a row in \mathbf{Y}' , each \mathbf{x}_i becomes a row in \mathbf{X} , and each \mathbf{e}_i becomes a row in \mathbf{E} . The matrix of feature vectors \mathbf{M} remains unchanged when moving to the multivariate model — different linear combinations of the same feature vectors reconstruct different waveforms. We write the multivariate version of this model as,

$$\mathbf{Y}'_{n \times t} = \mathbf{X}_{n \times p} \mathbf{M}_{p \times t} + \mathbf{E}_{n \times t}, \quad (7a)$$

$$\mathbf{e}_i \sim \mathcal{N}^C(\mathbf{0}, \mathbf{\Sigma}_R + \mathbf{\Sigma}_S). \quad (7b)$$

D. Parameterizing The Design Matrix

In this section, we summarize the methods we use for parameterizing the *design matrix* \mathbf{X} . This is a crucial aspect of the proposed multivariate regression model because the elements of \mathbf{X} define the linear combinations of the feature vectors in \mathbf{M} that reconstruct the catalog signals. The description of the physical parameters within the design matrix determines the interpretation of the resulting feature vectors.

Information on any kind of initial condition, characteristic quantity, and simulation parameters can be incorporated, such as the rotation rate of the inner core at bounce ($\beta_{ic,b}$), the equation of state, the differential rotation profile (A), or the inner core electron fraction at bounce.

The translation of physical parameters into a meaningful design matrix is known in the statistical literature as *variable encoding* (see, e.g., [35, 36]). The variable encoding techniques described and applied in this paper are a small sample of many possible encoding schemes.

1. Polynomial Encoding

In curve fitting, it is common to fit a curve to points in a two-dimensional scatter plot using polynomials of some specified order, allowing one to find evidence of trends in the data points. This approach is also useful in our multivariate model. For instance, we can imagine that as the rotation rate at core bounce changes, the presence of one of the feature vectors in the catalog waveforms changes in a correlated fashion.

To encode polynomial functions of a physical parameter into the design matrix, the actual values of the to-be-encoded physical parameter of the i th waveform are placed in the i th row of \mathbf{X} . The number of columns in \mathbf{X} devoted to encoding this parameter is equal to the order of the polynomial being used. In the first-order column, the parameter values are unchanged. In the second-order column, each of the parameter values is squared. In the third-order column, cubed, and so on. Each of these \mathbf{X} columns is associated with a feature vector in matrix \mathbf{M} .

Analogous to fitting a polynomial to a one dimensional curve, we fit a polynomial function of the parameters, expressed by the feature vectors in \mathbf{M} , to the set of waveforms \mathbf{Y} . Also note that an intercept term, or zeroth-order polynomial, is included. This manifests itself in the design matrix as a column in \mathbf{X} where each element is set to one. We denote a column in \mathbf{X} that is all ones as μ .

Each of the encodings described in this section includes a column of ones, but how this column is interpreted depends on the encoding. In a polynomial encoding, a column of ones in the design matrix produces a feature vector, \mathbf{m}_μ , that can be considered the constant term of our polynomial function of the physical parameters. Usually, little attention is given to the morphology of the intercept feature vector \mathbf{m}_μ , because $1 \cdot \mathbf{m}_\mu$ is present in the linear combination of feature vectors for every waveform reconstruction (or waveform prediction).

To illustrate the polynomial encoding, we will use a brief example. Assume we have a catalog with three waveforms, \mathbf{y}_1 , \mathbf{y}_2 , \mathbf{y}_3 , and that each waveform has a unique value for some continuous parameter called P . \mathbf{y}_1 has parameter P_1 , \mathbf{y}_2 has parameter P_2 and \mathbf{y}_3 has parameter P_3 . We wish to see whether we can find feature vectors that follow, for example, linear or quadratic trends in the waveforms. We can write out our second-order polynomial model, $\mathbf{Y} = \mathbf{X}_P \mathbf{M}$, explicitly,

$$\begin{pmatrix} \mathbf{y}_1 \\ \mathbf{y}_2 \\ \mathbf{y}_3 \end{pmatrix} = \begin{pmatrix} \mu & \text{linear} & \text{quadratic} \\ 1 & P_1 & P_1^2 \\ 1 & P_2 & P_2^2 \\ 1 & P_3 & P_3^2 \end{pmatrix} \begin{pmatrix} \mathbf{m}_\mu \\ \mathbf{m}_{\text{linear}} \\ \mathbf{m}_{\text{quadratic}} \end{pmatrix}.$$

Later in Secs. II E and II F, we use least squares to solve for the matrix of feature vectors \mathbf{M} as a linear combination of PCs.

While our multivariate regression model is linear in the sense that catalog waveforms are constructed by linear combinations of feature vectors, non-linear functions of the physical parameters can be used to produce those feature vectors. This allows for great flexibility in modeling the influence of physical parameters on rotating core collapse waveforms. Besides polynomials, other basis functions can be used, such as splines or radial basis functions [14].

Some parameters used to specify initial conditions for rotating core collapse are difficult to model continuously. For example, only five differential rotation profiles were employed by Abdikamalov *et al.* [19]. Polynomials may

not be the most suitable encoding. Also, it may be desirable to partition a parameter into several bins in order to see if there are particular feature vectors associated with, for instance, “low”, “medium”, or “high” parameter values. The following two types of variable encoding are devoted to discrete parameters. For example, Abdikamalov *et al.*, simulated the core collapse of progenitors where each had one of five differential rotation profiles.

2. Deviation Encoding

It is more straightforward to illustrate, instead of describe, a deviation encoding of the design matrix \mathbf{X} . For example, say we wish to partition a six-waveform catalog into three groups, defined by some physical parameter that takes on three values (or three ranges of values). Under a deviation encoding, waveforms in these groups (labeled by the subscripts g_1 , g_2 and g_3) are represented using three feature vectors; one for the mean of all catalog waveforms, labeled \mathbf{m}_μ ; one for the average difference from the mean of waveforms in g_1 , labeled $\mathbf{m}_{g_1-\mu}$; and one for the average difference of waveforms in g_2 , labeled $\mathbf{m}_{g_2-\mu}$. The average difference from the mean of g_3 waveforms is given by the negative of the sum of the g_1 and g_2 differences. We illustrate this encoding assuming there are a total of six waveforms in the catalog, two from each of the three groups. We write out this instance of $\mathbf{Y} = \mathbf{X}\mathbf{M}$ as,

$$\begin{pmatrix} \mathbf{y}_{1(g_1)} \\ \mathbf{y}_{2(g_1)} \\ \mathbf{y}_{3(g_2)} \\ \mathbf{y}_{4(g_2)} \\ \mathbf{y}_{5(g_3)} \\ \mathbf{y}_{6(g_3)} \end{pmatrix} = \begin{pmatrix} \mu & g_1 - \mu & g_2 - \mu \\ 1 & 1 & 0 \\ 1 & 1 & 0 \\ 1 & 0 & 1 \\ 1 & 0 & 1 \\ 1 & -1 & -1 \\ 1 & -1 & -1 \end{pmatrix} \begin{pmatrix} \mathbf{m}_\mu \\ \mathbf{m}_{g_1-\mu} \\ \mathbf{m}_{g_2-\mu} \end{pmatrix}.$$

Throughout the paper, we refer to the columns of \mathbf{X} , except the intercept term (μ), as *comparisons*. For instance, we can say that the second column of \mathbf{X} , $g_1 - \mu$, is a comparison between the mean of the g_1 waveforms and the mean of all six waveforms. If the mean of the g_1 waveforms is the same (or very similar) to the mean of all six waveforms, then the $\mathbf{m}_{g_1-\mu}$ feature vector will be insubstantial, or insignificant — many of the elements of $\mathbf{m}_{g_1-\mu}$ will be zero or very close to zero. This deviation encoding pattern is extensible to any number of groups, and any number of catalog waveforms.

3. Dummy Variable Encoding

A variation of deviation encoding expresses catalog waveforms as a difference from a specified reference group, instead of as a difference from the mean of the whole catalog. The name “dummy variable” refers to using ones as logical placeholders for actual parameter

values in the design matrix [35]. Using the same notation used previously, we designate the reference group in the next example to be g_1 . In the following case, each group is described as its difference from the average of the g_1 waveforms, instead of by its difference from the catalog mean. Explicitly, this is written as,

$$\begin{pmatrix} \mathbf{y}_{1(g_1)} \\ \mathbf{y}_{2(g_1)} \\ \mathbf{y}_{3(g_2)} \\ \mathbf{y}_{4(g_2)} \\ \mathbf{y}_{5(g_3)} \\ \mathbf{y}_{6(g_3)} \end{pmatrix} = \begin{pmatrix} \mu & g_2 - g_1 & g_3 - g_1 \\ 1 & 0 & 0 \\ 1 & 0 & 0 \\ 1 & 1 & 0 \\ 1 & 1 & 0 \\ 1 & 0 & 1 \\ 1 & 0 & 1 \end{pmatrix} \begin{pmatrix} \mathbf{m}_\mu \\ \mathbf{m}_{g_2-g_1} \\ \mathbf{m}_{g_3-g_1} \end{pmatrix},$$

The first column, μ , is the intercept term. In this dummy variable encoding, \mathbf{m}_μ , is the mean of the g_1 waveforms. The second column, $g_2 - g_1$, is a comparison of the mean of the g_1 group to the mean of the g_2 group. The feature vector $\mathbf{m}_{g_2-g_1}$ is therefore the difference between the mean of the g_2 and the g_1 waveforms. The third column, the $g_3 - g_1$ comparison, along with its feature vector, $\mathbf{m}_{g_3-g_1}$, is interpreted in a similar fashion. Linear combinations of the feature vectors determined by the design matrix reconstruct the six waveforms as

$$\begin{pmatrix} \mathbf{y}_{1(g_1)} \\ \mathbf{y}_{2(g_1)} \\ \mathbf{y}_{3(g_2)} \\ \mathbf{y}_{4(g_2)} \\ \mathbf{y}_{5(g_3)} \\ \mathbf{y}_{6(g_3)} \end{pmatrix} = \begin{pmatrix} \mathbf{m}_\mu \\ \mathbf{m}_\mu \\ \mathbf{m}_\mu + \mathbf{m}_{g_2-g_1} \\ \mathbf{m}_\mu + \mathbf{m}_{g_2-g_1} \\ \mathbf{m}_\mu - \mathbf{m}_{g_3-g_1} \\ \mathbf{m}_\mu - \mathbf{m}_{g_3-g_1} \end{pmatrix}.$$

As before, the g_1 subscript labels waveforms that are considered members of the g_1 group, and so on. As with the deviation encoding, this same encoding pattern is extensible to any number of waveform groups and any number of catalog waveforms.

4. Multiple Parameters and Interactions

Generally, more than one physical parameter is varied in core collapse simulations. As an example, imagine that we can partition our six waveforms as belonging to one of three groups, g_1 , g_2 or g_3 , as before. Additionally, the same set of waveforms can also be partitioned into one of two other groups, labeled h_1 and h_2 . For example, the three groups g_1 , g_2 and g_3 , might represent the fact that these waveforms were produced from progenitors with differential rotation A1, A2, and A3, respectively. The waveforms in groups h_1 and h_2 may then have come from progenitors with two different equations of state. Using a hypothetical waveform catalog with six waveforms as before, with two waveforms in each of the g groups and three waveforms in each of the h groups, we can construct a joint design matrix for both parameters.

To illustrate, we use the same deviation encoding on g shown in Sec. IID 2, and then choose a dummy variable

encoding on h , where \mathbf{y}_1 , \mathbf{y}_2 and \mathbf{y}_3 are members of h_1 , and the other three waveforms are members of h_2 . We choose our reference group to be h_2 . This design matrix, $\mathbf{X}_{g,h}$ is written explicitly as,

$$\mathbf{X}_{g,h} = \begin{pmatrix} \mu & g_1 - \mu & g_2 - \mu & h_2 - h_1 \\ 1 & 1 & 0 & 0 \\ 1 & 1 & 0 & 0 \\ 1 & 0 & 1 & 0 \\ 1 & 0 & 1 & 1 \\ 1 & -1 & -1 & 1 \\ 1 & -1 & -1 & 1 \end{pmatrix}.$$

Concatenating the encodings of different physical parameters (i.e. multiple groups) into the same design matrix allows us to consider the dependence of a waveform's morphology on different physical parameters as a linear combination of feature vectors, each attributable to one of the parameters. To help illustrate this subtle but important point, we write out explicitly how the feature vectors produced by the above design matrix construct the six example catalog waveforms,

$$\begin{pmatrix} \mathbf{y}_{1(g_1, h_1)} \\ \mathbf{y}_{2(g_1, h_1)} \\ \mathbf{y}_{3(g_2, h_1)} \\ \mathbf{y}_{4(g_2, h_2)} \\ \mathbf{y}_{5(g_3, h_2)} \\ \mathbf{y}_{6(g_3, h_2)} \end{pmatrix} = \begin{pmatrix} \mathbf{m}_\mu + \mathbf{m}_{g_1 - \mu} \\ \mathbf{m}_\mu + \mathbf{m}_{g_1 - \mu} \\ \mathbf{m}_\mu + \mathbf{m}_{g_2 - \mu} \\ \mathbf{m}_\mu + \mathbf{m}_{g_2 - \mu} + \mathbf{m}_{h_2 - h_1} \\ \mathbf{m}_\mu - \mathbf{m}_{g_1 - \mu} + \mathbf{m}_{g_2 - \mu} + \mathbf{m}_{h_2 - h_1} \\ \mathbf{m}_\mu - \mathbf{m}_{g_1 - \mu} + \mathbf{m}_{g_2 - \mu} + \mathbf{m}_{h_2 - h_1} \end{pmatrix}.$$

Once two encodings of two (or more) parameters, or groups, have been concatenated into the same design matrix, the interpretation of the feature vectors changes. For example, the feature vector $\mathbf{m}_{g_1 - \mu}$ is now interpreted as the average difference from the catalog mean of the waveforms in the g_1 group *after the removal of waveform morphology correlated with waveforms in either of the h groups*. Note also that in this example, \mathbf{m}_μ cannot be both the average of all catalog waveforms and the average of the waveforms in the h_1 group. It's precise physical meaning is difficult to qualify, especially as the complexity of the design matrix grows. It is best referred to as the "intercept feature vector".

In some cases, it may be desirable to consider *interactions* between groups, where an interaction defines the set of catalog waveforms that are members of multiple groups. For instance, we may be interested in features present only in waveforms that are considered members of one group *and* of a second group. Using the above example, we can produce feature vectors unique to waveforms in both g_1 and h_1 , and g_2 and h_1 , where we use the \times symbol to denote an interaction between two groups,

$$\mathbf{X}_{g,h,g \times h} =$$

$$\begin{pmatrix} \mu & g_1 - \mu & g_2 - \mu & h_2 - h_1 & g_1 \times h_1 & g_2 \times h_1 \\ 1 & 1 & 0 & 1 & 1 & 0 \\ 1 & 1 & 0 & 1 & 1 & 0 \\ 1 & 0 & 1 & 1 & 0 & 1 \\ 1 & 0 & 1 & 0 & 0 & 0 \\ 1 & -1 & -1 & 0 & 0 & 0 \\ 1 & -1 & -1 & 0 & 0 & 0 \end{pmatrix}.$$

An interaction column is computed easily by an element-wise multiplication of two columns in the design matrix [35]. A design matrix with a polynomial encoding can be concatenated with a design matrix with a dummy variable encoding, and interactions between a polynomial encoded independent variable and a deviation encoded variable are computed by an element-wise multiplication of design matrix columns. These two rules for producing interaction terms and modeling multiple groups concurrently applies to all encoding types [35]. In the above illustration, we created what is called a *two-way interaction* between two different parameter types. By multiplying more than two design matrix columns together at a time, higher order interactions terms can be defined.

E. Factoring M with Singular Value Decomposition

In the previous sections, \mathbf{M} is treated as an unknown matrix of physically meaningful feature vectors which can be used to reconstruct each of the waveforms \mathbf{y}_i . At this point, we can estimate the $p \cdot t$ matrix elements in \mathbf{M} by solving the matrix equation $\mathbf{Y} = \mathbf{X}\mathbf{M}$ using least squares. For convenience, p is the number of columns in \mathbf{X} , k is the number of PCs in \mathbf{Z}^\dagger , and t is the number of samples per waveform in \mathbf{Y} .

However, reducing the number of statistical parameters (elements of \mathbf{M}) that need to be estimated greatly reduces the degrees of freedom and enables the apparatus of statistical hypothesis testing (see Sec. II C for further details on hypothesis testing). To reduce the number of matrix elements that need to be estimated, we factor \mathbf{M} into two matrices in such a way that our feature vectors are expressed as linear combinations of PCs. Given a PC basis, this unknown matrix is comprised of $p \cdot k$ PC coefficients, where $p \cdot k \ll p \cdot t$. Refs. [10, 16] have shown that for n rotating core collapse waveforms, only $k \ll n$ basis vectors are needed to provide excellent reconstructions of a large majority of waveforms of the catalog.

To construct the PC basis, we follow previous work [10, 13, 16] and apply singular-value decomposition (SVD) to factorize our matrix of Fourier-transformed waveforms, \mathbf{Y} , into three matrices,

$$\mathbf{Y} = \mathbf{U}\mathbf{S}\mathbf{V}^\dagger, \quad (8)$$

where the rows of \mathbf{V}^\dagger are the eigenvectors of the matrix $\mathbf{Y}^\dagger \mathbf{Y}$ and are called principal components (PCs), which form an orthonormal basis for \mathbf{Y} . The PCs obtained in this fashion are equivalent to those obtained by applying

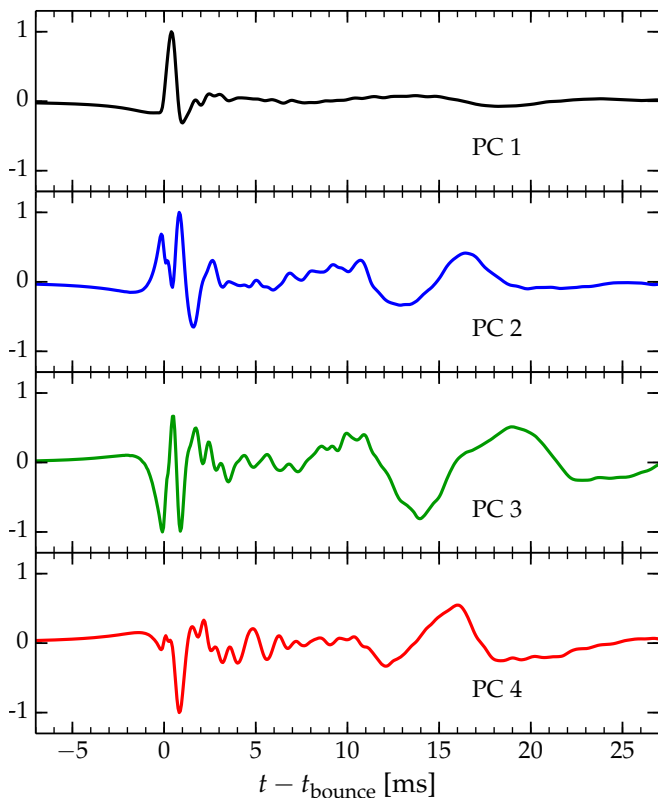


FIG. 2. The first four principal components (PCs) from the waveforms of the Abdikamalov *et al.* catalog in the time domain. Each PC has been normalized by its maximum amplitude.

SVD to the time domain waveforms, Fourier transforming the time domain PCs, then normalizing the PCs with the multiplicative constant $t_s^{-1/2}$, where t_s is the number of time samples per time domain waveform. Figure 2 depicts the first four PCs computed from the Abdikamalov *et al.* catalog [19].

Past work [10, 13, 16, 37] used SVD in the following fashion to form a basis from which GWs are reconstructed: To be exact, the i th catalog waveform is represented as a linear combination of k basis vectors. We denote the $1 \times k$ vector of coefficients of this linear combination by \mathbf{a} , and the PC basis by \mathbf{Z} , whose columns are the first k PCs. Each \mathbf{y}_i is approximated by,

$$\mathbf{y}_i \approx \sum_{j=1}^k a_j \mathbf{Z}_j, \quad (9)$$

where \mathbf{Z}_j is the j th basis vector of the PC basis \mathbf{Z} and a_j is the corresponding reconstruction coefficient.

Instead of directly representing catalog waveforms with linear combinations of PCs, our multivariate regression model represents the feature vectors that characterize physical parameters as linear combinations of PCs. Subsequently, catalog waveforms are represented by linear combinations of these feature vectors, where each feature vector is a row in \mathbf{M} . To express this relationship

between the catalog waveforms and the PC basis, we factor \mathbf{M} into a known and an unknown part,

$$\mathbf{M}_{p \times t} = \mathbf{B}_{p \times k} \mathbf{Z}^\dagger_{k \times t}, \quad (10)$$

where the rows of \mathbf{Z}^\dagger are the k PCs. Since all other matrices, \mathbf{Y} , \mathbf{X} , and \mathbf{Z}^\dagger , are known, what remains is to find a solution for the $p \times k$ elements of \mathbf{B} , which we will obtain below via a least-squares fit.

Casting our feature vectors as linear combinations of PCs is beneficial in two ways. First, we bridge between the past work of [10, 13, 16] to the physical parameters of collapse, whose relationship to GW morphology is of great interest. Second, using the PC basis enables the apparatus of statistical hypothesis testing by dramatically reducing the number of statistical parameters that need to be estimated (see Sec. II G). Test statistics and hypothesis testing can be used to measure the magnitude of a feature vector associated with a physical parameter.

After the feature matrix \mathbf{M} has been factored into \mathbf{B} and \mathbf{Z}^\dagger , we rewrite Eq. 7a with $\mathbf{E} = [\mathbf{e}_1^T \mathbf{e}_2^T \dots \mathbf{e}_n^T]^T$ as

$$\mathbf{Y}'_{n \times t} = \mathbf{X}_{n \times p} \mathbf{B}_{p \times k} \mathbf{Z}^\dagger_{k \times t} + \mathbf{E}_{n \times t}. \quad (11)$$

We note here that it is equivalent to speak about rows of \mathbf{B} or rows of \mathbf{M} for referring to feature vectors associated with physical parameters because each row of \mathbf{B} defines the linear combination of PC basis vectors that construct the corresponding feature vector in \mathbf{M} .

F. The Least Squares Solution

With all the ingredients that are required to specify our linear model at hand, we can move to estimating the unknown quantities in Eq. 11, \mathbf{B} and Σ_R . We denote estimators for the unknown quantities with a caret ($\hat{\cdot}$), while the *true* value of an unknown quantity has the same bold notation as known vectors and matrices. In this section, we provide the known analytic solutions for these estimators, which maximize the complex multivariate Gaussian likelihood function over the residuals [31, 32]. Maximizing this likelihood function is equivalent to minimizing the sum of squares of the elements of the residuals \mathbf{R} , where $\mathbf{R} = \mathbf{Y} - \mathbf{X}\hat{\mathbf{B}}\mathbf{Z}^\dagger$. In other words, our estimate of \mathbf{B} , denoted $\hat{\mathbf{B}}$, minimizes the quantity,

$$\|\mathbf{Y}' - \mathbf{X}\hat{\mathbf{B}}\mathbf{Z}^\dagger\|^2, \quad (12)$$

where from Eq. 5, each $\mathbf{y}'_i = \mathbf{y}_i + \mathbf{s}_i$. The estimate of \mathbf{B} which minimizes the above expression is given analytically [31, 32],

$$\hat{\mathbf{B}} = (\mathbf{X}^T \mathbf{X})^{-1} \mathbf{X}^T \mathbf{Y}' \mathbf{Z} (\mathbf{Z}^\dagger \mathbf{Z})^{-1}. \quad (13)$$

Equation 13 can be simplified in two ways. Since the PCs produced from the SVD form an orthonormal basis

set, $\mathbf{Z}^\dagger \mathbf{Z} = \mathbf{I}_t$, the $t \times t$ identity matrix, where t is the number of data samples in each of the waveforms. We can also factor the least squares solution for \mathbf{B} into two parts, remembering that each $\mathbf{y}'_i = \mathbf{y}_i + \mathbf{s}_i$. This factored least squares estimator is written as,

$$\hat{\mathbf{B}} = \mathbf{C}\mathbf{X}^T\mathbf{Y}\mathbf{Z} + \mathbf{C}\mathbf{X}^T \begin{bmatrix} \mathbf{s}_1^T & \mathbf{s}_2^T & \dots & \mathbf{s}_n^T \end{bmatrix}^T \mathbf{Z}, \quad (14)$$

where $\mathbf{C} = (\mathbf{X}^T \mathbf{X})^{-1}$. Instances of detector noise \mathbf{s}_i are unrelated to the model residual \mathbf{R} , and from Eq. 4, each of their expectation values is the zero vector ($\mathbb{E}(\mathbf{s}_i) = \mathbf{0}$). Therefore, we can drop the detector noise contribution to the estimator and set $\mathbf{Y}' = \mathbf{Y}$. Equation 13 simplifies to

$$\hat{\mathbf{B}}_{p \times k} = \mathbf{C}\mathbf{X}^T\mathbf{Y}\mathbf{Z}, \quad (15)$$

where p is the number of columns of \mathbf{X} , and k is the number of PCs in \mathbf{Z}^\dagger . Now that we have an estimate $\hat{\mathbf{B}}$ for \mathbf{B} , we can use our multivariate regression model to generate waveforms with arbitrary values of the physical parameters determined by our choice of the design matrix \mathbf{X} .

To obtain *reconstructions* of the catalog waveforms \mathbf{Y} , we can write,

$$\mathbf{Y}^R = \mathbf{X}\hat{\mathbf{B}}\mathbf{Z}^\dagger \quad (16)$$

where the reconstructed waveforms are denoted \mathbf{Y}^R . To *predict* a waveform from a progenitor with different parameter values than any of the original catalog waveforms, we encode its physical parameters into a vector $\tilde{\mathbf{x}}$ in the same fashion as the original \mathbf{X} was encoded and write,

$$\tilde{\mathbf{y}} = \tilde{\mathbf{x}}\hat{\mathbf{B}}\mathbf{Z}^\dagger \quad (17)$$

where $\tilde{\mathbf{y}}$ is the expected waveform predicted from our regression model. In Eq. 17, \mathbf{X} , $\hat{\mathbf{B}}$ and \mathbf{Z}^\dagger are derived from the original waveform set.

We can also use our regression model to examine how influential certain physical parameters are on catalog morphology. In Sec. IID, we saw how our encodings of the design matrix led to $\mathbf{B}\mathbf{Z}^\dagger$ being interpretable as a feature matrix \mathbf{M} , where each of the feature vectors in \mathbf{M} is associated with a column of the design matrix \mathbf{X} . If the comparison defined by the i th column of \mathbf{X} is insignificant to waveform morphology, then we would expect the magnitude of the i th feature vector in \mathbf{M} to be small. For the feature vector to have a small magnitude, the elements in the i th row of \mathbf{B} must be zero or close to zero. Therefore, we can measure how important various parameters are to catalog morphology by looking closely at the magnitude of the elements of our estimator of \mathbf{B} . In the following section, we give test statistics based on the values of $\hat{\mathbf{B}}$ that are useful for measuring how influential particular physical parameters are on catalog morphology.

G. Statistical Hypothesis Testing

In a statistical hypothesis test, two hypotheses are proposed, a null hypothesis and its alternative hypothesis [38]. In our situation, they can be summarized as follows:

- Null Hypothesis, H_0 : Relevant elements of $\mathbf{B} = \mathbf{0}$;
- The Alternative, H_a : Relevant elements of $\mathbf{B} \neq \mathbf{0}$.

In this paper, we are primarily interested in whether specific feature vectors (rows of \mathbf{B}), are equal to the zero vector. In this case, our H_0 is that all the elements in a particular row of \mathbf{B} are equal to zero. Occasionally, we may be interested in whether one of the PC basis vectors is influential in a given feature. In that case, our H_0 is that a particular element of \mathbf{B} is equal to zero. We describe in detail the procedure for conducting hypothesis tests on the rows of \mathbf{B} in Sec. IIG 3. The procedure for testing individual elements is given in Sec. IIG 4.

1. An Illustration

The evidence in favor of, or against, some null hypothesis (H_0) depends not just on the magnitudes of the elements of \mathbf{B} in question, but also on the covariances of the waveforms. Additionally, the number of waveforms also plays a role. As a simple example, imagine we have put a dummy variable encoding on a set of waveforms whose parameters can be grouped into three groups labeled g_1 , g_2 , and g_3 . We are interested in whether there is a significant difference between the g_2 and g_1 waveforms. This is the scenario described in Sec. IID 3.

In this scenario, the feature vector $\mathbf{m}_{g_2-g_1}$ produced from the design matrix is the average of the differences between the g_2 and the g_1 waveforms. Our H_0 is that the elements in this row of \mathbf{B} , the PC coefficients that construct the feature vector $\mathbf{m}_{g_2-g_1}$, are all equal to zero — there is no difference, on average, between the g_2 and g_1 waveforms. Imagine we find that the magnitudes of these PC coefficients are somewhat large, leading to a substantial feature vector $\mathbf{m}_{g_2-g_1}$. This result provides evidence against H_0 .

However, if the morphology of this set of g_2 and g_1 waveforms is very heterogeneous, then our evidence against H_0 diminishes. Noting a large difference between two sets of highly variable waveforms is less compelling than if the waveforms within each of the two sets were very similar to each other. We construct the covariance matrix for the residuals below in Sec. IIG 2.

The number of g_1 or g_2 waveforms generated also matters. Imagine we obtain a substantial feature vector, and the morphology of the two sets of waveforms is reasonably homogeneous. However, if there were only two g_2 and two g_1 waveforms, it is less reasonable to claim that g_2 and g_1 waveforms are significantly different than if there were 20 g_2 and 20 g_1 waveforms. This type of information is

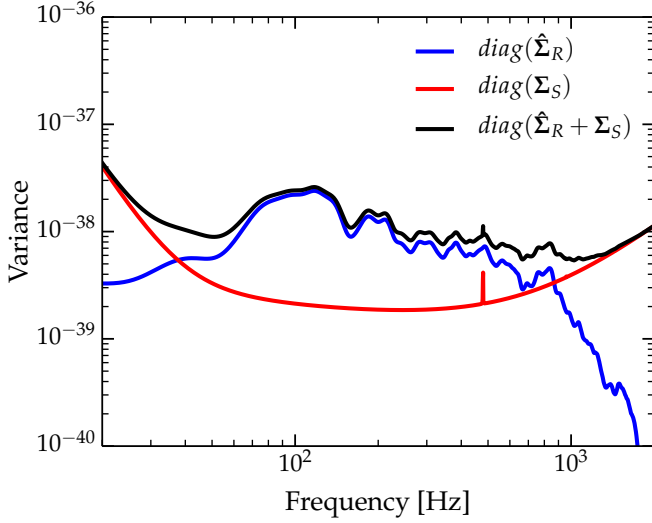


FIG. 3. The diagonal of $\hat{\Sigma}_R$, Σ_S , and the sum of $\hat{\Sigma}_R$ and Σ_S . We set the diagonal elements of Σ_S to the Advanced LIGO noise variances. In producing $\hat{\Sigma}_R$, the catalog waveforms have been scaled to a distance of 10 kpc, and we used a design matrix with a deviation encoding on the 5 differential rotation profiles. As the waveforms are scaled to greater distances, the noise curve variances will begin to dominate over the residual variances.

captured by the inverse of the covariance matrix of the design matrix, $\mathbf{C} = (\mathbf{X}^T \mathbf{X})^{-1}$, which factors into the test statistics.

2. Estimating the Covariance of the Residuals

We express the level of heterogeneity of the morphology of a set of waveforms with a covariance matrix on the residuals of our fit and the original catalog waveforms. The matrix of residuals, \mathbf{R} , can be computed by,

$$\mathbf{R} = \mathbf{Y} - \mathbf{X}\hat{\mathbf{B}}\mathbf{Z}^\dagger. \quad (18)$$

From [31, 32], we obtain an estimator for the covariance of the residuals, Σ_R , as

$$\hat{\Sigma}_R = \frac{1}{n-p} \mathbf{R}^\dagger \mathbf{R}, \quad (19)$$

where n is the number of catalog waveforms, and p is the number of columns of \mathbf{X} .

We also want to include uncertainty due to detector noise in our inferences. From Eq. 6b, we can add the detector noise covariance matrix (described in Eq. 4) to obtain our estimate of the total error covariance, due to the combined hypothetical detector noise and the residuals, $\hat{\Sigma}_E$,

$$\hat{\Sigma}_E = \hat{\Sigma}_R + \hat{\Sigma}_S. \quad (20)$$

In Fig. 3, we graphically compare the diagonals of $\hat{\Sigma}_R$ and Σ_S . To produce this plot, we used a design matrix

with a deviation encoding on the five values of differential rotation. At a common source distance of 10 kpc, the variance due to the residuals remains dominant over the variances due to the Advanced LIGO design noise curve in the zero-detuning, high-power configuration [29].

While the elements of our solution \mathbf{B} are PC coefficients, the elements of $\hat{\Sigma}_R$ are the residual variance and covariances between residual frequency bins. We change the basis of $\hat{\Sigma}_R$ into the same PC basis as our solution \mathbf{B} in order to estimate the total error covariance in our test statistics [31],

$$\hat{\Sigma}_Z = \mathbf{Z}^\dagger \hat{\Sigma}_E \mathbf{Z}, \quad (21)$$

where the total error covariance in terms of the PC basis is $\hat{\Sigma}_Z$. We use this result in the construction of both Hotelling's T^2 and student's t test statistics.

3. Hotelling's T^2 — Inferences Regarding Rows of \mathbf{B}

We are often interested in whether all the elements in a specific row of $\hat{\mathbf{B}}$ are equal to zero. This is because each row of $\hat{\mathbf{B}}$ determines how influential to catalog morphology each column of the design matrix is. We use the variable $\hat{\mathbf{b}}_i$ to represent a selected row. This particular test statistic is known as the Hotelling's T^2 statistic [39], and is given by,

$$T^2 = \frac{\hat{\mathbf{b}}_i \hat{\Sigma}_Z^{-1} \hat{\mathbf{b}}_i^\dagger}{\mathbf{C}_{ii}}, \quad (22)$$

where \mathbf{C}_{ii} is the i th diagonal element of $\mathbf{C} = (\mathbf{X}^T \mathbf{X})^{-1}$. The matrix \mathbf{C} contains information regarding the number of waveforms, as per the discussion in Sec. II G 1. Under H_0 (all elements in $\mathbf{b}_i = \mathbf{0}$), it can be shown that this statistic can be written in terms of the \mathcal{F} -distribution [31, 32],

$$\frac{v-k+1}{vk} T^2 \sim \mathcal{F}_{2k, 2(v-k+1)}, \quad (23)$$

where $v = n - p$, n is the number of waveforms in \mathbf{Y} , p is the number of columns of \mathbf{X} , and k is the number of PCs in \mathbf{Z}^\dagger . The tilde (\sim) can be read as “is distributed as”. $2k$ is the “upper” degrees of freedom in the \mathcal{F} distribution [40], and $2(v-k+1)$ is the “lower” degrees of freedom. We delay a brief discussion of the details and use of these test statistics until Sec. II G 5.

Hotelling's T^2 statistic is valid if and only if $v \geq k$, necessitating the use of our PC basis \mathbf{Z}^\dagger in the statistical model (see Sec. II E). If there were no basis used (i.e., \mathbf{Z}^\dagger is set to the $t \times t$ identity matrix), then $k = t$ in Eq. 23, where t is the number of data samples in each waveform, p is the number of design matrix columns and k is the number of PCs in \mathbf{Z}^\dagger . In this case, $v = n - p$ is not greater than or equal to k , causing the left hand side of Eq. 23 to be negative — outside the domain of the \mathcal{F} -distribution. The constraint $v \geq k$ cannot be satisfied unless the waveforms are reconstructed with a basis that is smaller than

the size of the catalog. Thus using a PC basis not only allows us to connect PCs to physical parameters, but also enables statistical hypothesis testing.

4. The Student's t Statistic — Testing Elements of $\hat{\mathbf{B}}$

We may also be interested in testing whether individual elements of \mathbf{b}_i (rows of \mathbf{B}) are equal to zero. Each of the k elements of \mathbf{b}_i are coefficients defining a linear combination of PC basis vectors \mathbf{Z}^\dagger that construct each row of the feature matrix \mathbf{M} linking physical parameters of rotating core collapse and principal components (PCs). Hypothesis tests on elements allow us to measure how important individual PCs are to a given feature vector.

We use the complex form of the student's t test statistic [30, 41], given by

$$\tau = \frac{|\hat{\mathbf{B}}_{i,j}|^2}{\mathbf{C}_{ii} \hat{\Sigma}_{Z_{jj}}}, \quad (24)$$

where $\hat{\Sigma}_{Z_{jj}}$ is the j th diagonal element of $\hat{\Sigma}_Z$. For the real case, see [31]. Under H_0 ($\mathbf{B}_{i,j} = 0$), the distribution of this test statistic is given by,

$$\frac{1}{2}\tau \sim \mathcal{F}_{2,2v}, \quad (25)$$

where 2 is the upper degrees of freedom parameter, and $2v$ is the lower degrees of freedom parameter of the \mathcal{F} -distribution. This test statistic can easily be used to produce circular confidence intervals for each element of $\hat{\mathbf{B}}$ in the complex plane (e.g., see Fig. 5).

5. Discussion of Test Statistics

The complex forms of both the Hotelling's T^2 and the student's t statistics are distributed according to the \mathcal{F} -distribution (also known as the Fisher-Snedecor probability distribution, see [40]). The factors of two in the degrees of freedom parameters in Eqs. 23 and 25 come from the fact that our Fourier transformed waveforms are complex valued. For a derivation of Hotelling's T^2 statistic and student's t statistic in the real-valued case, see [31] and references therein. For the Hotelling's T^2 with complex data, see [32].

To compute η in practice, the results of either Eqs. 22 or 24 are plugged into the left hand side of either Eqs. 23 or 25. We label the quantity obtained η . Next, η is transformed into a p -value, which is more easily interpreted. A p -value is the probability, under the assumption that H_0 is true, of obtaining an η value as high as or higher than was computed. For a more detailed summary on the precise interpretation and computation of p -values, see [38]. The p -value transform is defined as,

$$p\text{-value} = \int_{\eta}^{\infty} f(x; df_{upper}, df_{lower}) dx, \quad (26)$$

where $f(x; df_{upper}, df_{lower})$ is the \mathcal{F} -distribution function, df_{upper} is the upper degrees of freedom, and df_{lower} is the lower degrees of freedom. Keeping in mind that if H_0 is true, η values will be distributed according to the probability distribution function $f(x; df_{upper}, df_{lower})$. Therefore obtaining a small p -value indicates a lack of evidence for H_0 . In this paper, we consider p -values at or below 0.01 *significant*, where *significant* indicates that we reject H_0 and favor H_a .

We note here that it is simple to alter our regression model for waveforms that have not been Fourier transformed. With real-valued time domain waveforms, one would follow all the same procedures described, but would drop the detector noise covariance matrix, Σ_S , and remove the factor of two from the degrees of freedom in Eqs. 23 and 25. This is the only alteration to the regression model and hypothesis testing method that would need to be made in order to analyze, reconstruct, and predict time domain waveforms.

III. STATISTICAL ANALYSIS OF THE ABDIKAMALOV *ET AL.* WAVEFORM CATALOG

With relevant statistical modeling procedures accounted for, we move on and present an analysis of the rotating core collapse GW signal catalog of Abdikamalov *et al.* ([19] and section II A). Before beginning an analysis, the set of waveforms \mathbf{Y} must be scaled to a common distance. Throughout the remainder of the paper, we scale all waveforms to the distance of 10 kpc in each of our analyses.

Abdikamalov *et al.* [19] studied how varying rotational parameters (e.g., rotation parameter $\beta_{ic,b}$ of the inner core at bounce and precollapse degree of differential rotation A) affect the morphology of the emitted GWs. Using a series of design matrices, we shall gradually develop a multivariate regression model of how changes in the rotational parameters correlate with waveform catalog morphology.

Throughout the remainder of this paper, we use 7 PCs in our PC basis \mathbf{Z}^\dagger ($k = 7$) unless stated otherwise. This choice is motivated by Logue *et al.* [16]. Experiments with more PCs show that the results remain essentially the same up to ~ 20 PCs, beyond which individual higher-order PCs contribute little to the actual signal feature vectors and add degrees of freedom that decrease the significance of results. We leave a more detailed study of the sensitivity of our results to the number of employed PCs to future work.

A. Analyzing Differential Rotation

We begin our analysis of the Abdikamalov *et al.* waveform catalog with comparisons of the waveforms grouped by their 5 differential rotation profiles in order to see how much they differ from waveforms in the other groups on

TABLE I. Results of pair-wise comparisons between waveforms with different differential rotation profiles. An asterisk (*) marks results that are considered significant (large values of T^2 producing p -values at or below 0.01 are considered “significant”). The waveforms are all scaled to be at the common distance of 10 kpc. $Ai - Aj$ indicates that we are measuring the average difference between waveforms from cores with the Ai differential rotation profile, and waveforms from cores with the Aj differential rotation profile.

Comparison	Hotelling’s T^2	p -value
$A1 - A2$	26.63	$4.4 \times 10^{-5}*$
$A1 - A3$	26.46	$4.8 \times 10^{-5}*$
$A1 - A4$	23.78	$2.1 \times 10^{-4}*$
$A1 - A5$	18.67	0.003*
$A2 - A3$	6.35	0.62
$A2 - A4$	16.22	0.01*
$A2 - A5$	17.01	0.008*
$A3 - A4$	5.58	0.73
$A3 - A5$	7.57	0.45
$A4 - A5$	0.98	0.999

average. This allows us to measure the average difference between waveforms generated from progenitors with different differential rotation setups.

The procedure to obtain these results, given in Table I, is as follows: First, we apply a dummy variable encoding on differential rotation and form four different design matrices, each with a different reference group left out (Section IID3 details this step). With the first design matrix, we measure the significance of the difference between the $A1$ and the $A2$ waveforms (denoted in Tab. I as $A1 - A2$), the $A1$ and the $A3$ waveforms, the $A1$ and the $A4$ waveforms, and the $A1$ and $A5$ waveforms. In this design matrix, the $A1$ waveforms are the reference group. The other three design matrices have $A2$, $A3$, and $A4$ as their reference group, respectively, and account for all remaining possible comparisons.

Under a dummy variable encoding of a parameter, the elements in each row of \mathbf{B} are the PC coefficients that produce the average difference between waveforms from progenitors with two differential rotation profiles. Hotelling’s statistic (Eq. 22) tests all the elements of $\hat{\mathbf{b}}_i$ simultaneously. We list both Hotelling’s statistic, and the p -value derived from it. Sometimes, we may find that two (or more) comparisons have highly significant p -values that are numerically equivalent to zero. In this situation, the value of T^2 can be used to measure the difference in significance between the two comparisons.

We find no evidence in Tab. I for a significant difference between waveforms with differential rotation $A2$ and $A3$ ($A2 - A3$), $A3$ and $A4$ ($A3 - A4$), $A3$ and $A5$ ($A3 - A5$), as well as $A4$ and $A5$ ($A4 - A5$). Differences are more significant for comparisons that involve waveforms from more differentially rotating progenitors. Each comparison involving the $A1$ group is significant, and most of

TABLE II. Testing the average difference between a set of waveforms partitioned by differential rotation profile and the mean of all catalog waveforms. An asterisk (*) marks results that are considered significant (large values of T^2 producing p -values at or below 0.01 are considered “significant”). All waveforms are scaled to be at the common distance of 10 kpc. Our results show that the $A1$ and to a lesser extent, the $A2$ waveforms are significantly different from the average of all catalog waveforms.

Comparison	Hotelling’s T^2	p -value
$A1 - \mu$	38.54	$6.3 \times 10^{-8}*$
$A2 - \mu$	19.48	0.002*
$A3 - \mu$	6.67	0.57
$A4 - \mu$	7.67	0.44
$A5 - \mu$	8.01	0.39

the comparisons involving $A2$ are as well. This suggests that for a detected core collapse GW signal, it may be possible to determine either that its source was strongly differentially rotating (most similar to $A1$ or $A2$) or that its source had a more moderate degree of differential rotation (most similar to the $A3$, $A4$ and $A5$ parameterizations).

The significance of comparisons that involve $A1$ decreases as the differential rotation of the comparison waveforms decreases. This does not necessarily suggest that $A1$ waveforms are more similar to waveforms from more uniformly rotating progenitors than to those with similar differential rotation profiles. The T^2 value (and therefore p -values transformed from it) is dependent not only on the intrinsic difference between the waveforms in each of the groups being compared, but also on the numbers of waveforms in each of the groups. There are 30 $A1$ waveforms, 22 $A2$ waveforms, 18 $A3$ waveforms, 12 $A4$ waveforms, and 10 $A5$ waveforms in the Abdikamalov *et al.* catalog. As we remarked in Sec. IIC, the \mathbf{C}_{ii} term in Hotelling’s T^2 is responsible for characterizing the relative scaling of the design matrix columns. There is more support for the significance of a comparison if there is a large number of waveforms in each of the two groups being compared. The evidence for significance is driven down when one (or both) of the groups in a comparison has a small number of waveforms.

To consider how influential different degrees of differential rotation are individually, we examine how the GWs from each group compare to the overall catalog mean. A deviation encoding allows us to measure how *unique* a signature in the waveforms produced with a given parameter value is, without having to use a set of waveforms with another parameter value as a reference. This is accomplished with a deviation encoding of the differential rotation parameter (see Sec. IID). In Table II, we list Hotelling’s T^2 and the corresponding p -value results of comparisons of the differential rotation parameter groups with the catalog mean. In Tab. II, the μ symbol denotes the intercept term, the mean of all the catalog waveforms.

The results in Tab. II corroborate the results in Tab. I. We find that the A1 and A2 groups indeed produce the most unique signature. Waveforms from the A1 group are on average the most different from the mean of the catalog waveforms (depicted in Fig. 1). This also supports the conclusions about the impact of differential rotation drawn by Abdikamalov *et al.* [19].

In order to visualize the results of Tab. II, we estimate the uncertainty of $\hat{\mathbf{M}}$ in the time domain using the estimated standard deviations of the elements of $\hat{\mathbf{B}}$, given by $\mathbf{C}_{ii}\hat{\Sigma}_{Z_{jj}}$. For the comparisons listed in any of our tables that have lower p -values, we can expect to see smaller estimated errors in their corresponding estimated feature vectors. The top panel of Fig. 4 shows the feature vector that corresponds to the $A1 - \mu$ column of a design matrix comprised of a deviation encoding on differential rotation. When testing the row of $\hat{\mathbf{B}}$ that produces this feature vector, we obtain a p -value of 6.3×10^{-8} (the first row of Tab. II). The bottom panel of Fig. 4 is the feature vector that represents $A3 - \mu$, for which we obtain a p -value of 0.57. The $A1 - \mu$ feature vector is the most significant in Tab. II, and the $A3 - \mu$ feature vector is the least significant. Both time domain feature vectors are plotted with 3σ error regions. As the p -value results suggest, the $A1 - \mu$ time domain feature vector has both a larger amplitude and a narrower error region.

B. The Influence of Total Rotation

Abdikamalov *et al.* [19] observed that the morphology of the waveforms in their catalog is highly dependent on the ratio of rotational kinetic energy to gravitational energy of the inner core at bounce, $\beta_{ic,b}$, where the subscript ic,b stands for “inner core, at bounce”. This parameter is a good measure of the progenitor core’s *total rotation* [19], and continuously varies from $\beta_{ic,b} = 0.0016$ to $\beta_{ic,b} = 0.206$ throughout the Abdikamalov *et al.* catalog. In this section, we examine results using design matrices parameterized by total rotation. We bin $\beta_{ic,b}$ into three groups, corresponding to slow, moderate and rapid rotation. We use the labels S, M, R to denote this:

- $\beta S = [0.0016, 0.0404]$, 30 waveforms;
- $\beta M = [0.0414, 0.1096]$, 31 waveforms;
- $\beta R = [0.115, 0.206]$, 31 waveforms.

We choose these ranges based on Fig. 10 of Abdikamalov *et al.* [19]. These ranges are approximately ranges over which $\beta_{ic,b}$ produces qualitatively similar behavior in three of the primary waveform peaks [19].

We begin an analysis of total rotation by using a dummy variable encoding on our three total rotation ranges. The results of this encoding are shown in Table III. The results in this table show that total rotation is much more influential on GW morphology than differential rotation. The values of T^2 (and their p -values) show a dramatic increase in significance compared to the

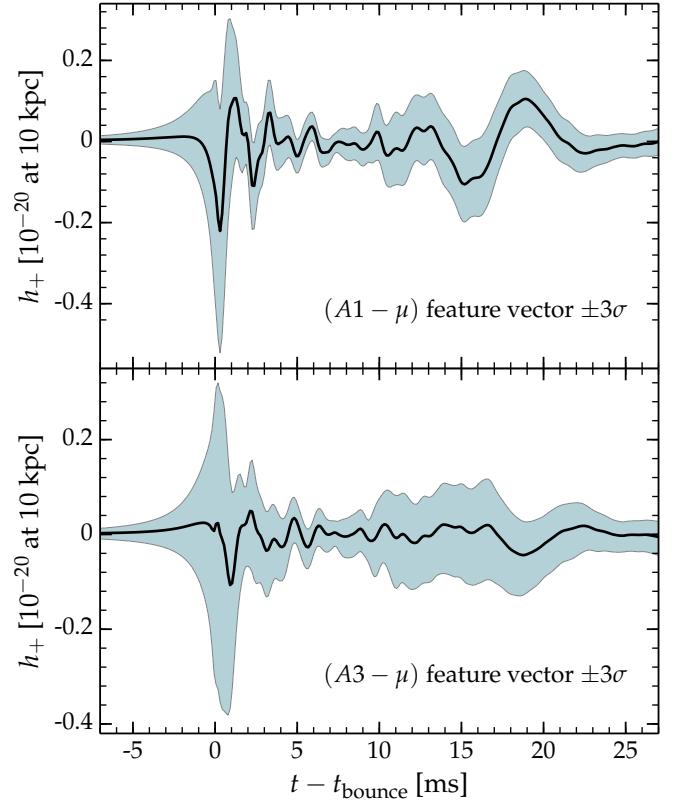


FIG. 4. Two time domain feature vectors shown with a 3σ confidence region produced using the deviation encoded design matrix used in Tab. II. The top panel shows the $A1 - \mu$ feature vector. The large amplitudes between about 10 and 20 milliseconds in the A1 feature vector suggests that the A1 waveforms differ significantly from the catalog mean in that phase. The bottom panel shows the $(A3 - \mu)$ feature vector. The wider confidence region indicates the lack of a robust feature vector that can be used to characterize the difference between the A3 waveforms from the catalog mean. To produce these feature vectors, the waveforms in the catalog were originally scaled to a distance of 10 kpc.

results in Tables I and II. This means that differences in waveform morphology are much more pronounced when partitioning waveforms by $\beta_{ic,b}$. The p -values obtained for every comparison are equal to zero, to machine precision, and the values of Hotelling’s T^2 are exceptionally large.

These results suggest that parameter estimation methods should be able to accurately measure the total rotation from a rotating core collapse GW signal detected by Advanced LIGO. This is in agreement with Abdikamalov *et al.* [19], who use a match filtering parameter estimation approach [34] to measure $\beta_{ic,b}$ to within $\sim 30\%$ of its true value. They also show that $\beta_{ic,b}$ can be directly related to the total angular momentum of the inner core at bounce. Thus the ability to measure $\beta_{ic,b}$ provides a straightforward way to determine the angular momentum content in the core of a collapsing star.

TABLE III. Results of comparisons between waveforms partitioned into three groups based on $\beta_{ic,b}$, a parameter expressing the total rotation of the inner core at bounce. While all comparisons marked with an asterisk (*) are significant (p -value ≤ 0.01), a larger value of T^2 can be used to determine how different from each other waveforms from different groups are, since all comparisons produced p -values numerically equivalent to zero. All waveforms are scaled to a distance of 10 kpc. βi indicates one of three ranges of $\beta_{ic,b}$ (see text for details). $\beta i - \beta j$ indicates that we are measuring the average difference between the sets of waveforms from progenitors with the βi and the sets of waveforms from progenitors with the βj total rotation.

Comparison	Hotelling's T^2	p -value
$\beta S - \beta M$	132.7	0.0*
$\beta S - \beta R$	311.7	0.0*
$\beta M - \beta R$	205.0	0.0*

TABLE IV. Results of comparisons between waveforms grouped by different ranges of $\beta_{ic,b}$ and values of A , and the catalog mean. Both parameters were simultaneously encoded in the design matrix. The waveform catalog is originally scaled to a distance of 10 kpc. $Ai - \mu$ or $\beta i - \mu$ indicates that we are measuring the average difference between that set of waveforms and the average of all catalog waveforms. An asterisk (*) marks results that are considered significant (large values of T^2 producing p -values at or below 0.01 are considered “significant”).

Comparison	Hotelling's T^2	p -value
$A1 - \mu$	49.7	2.0×10^{-10} *
$A2 - \mu$	18.1	4.4×10^{-3} *
$A3 - \mu$	9.2	0.27
$A4 - \mu$	8.5	0.34
$A5 - \mu$	6.0	0.67
$\beta S - \mu$	260.4	0.0*
$\beta M - \mu$	117.8	0.0*
$\beta R - \mu$	309.6	0.0*

Next, we test solutions from design matrices that are a concatenation of a deviation encoding on the three ranges of $\beta_{ic,b}$, and a deviation encoding on the five levels of differential rotation ($A1$ through $A5$). For more details on this type of procedure, see Section IID 4. This scheme improves our inferences on both the differential and total rotation parameters because it produces a solution where the effects of the two types of parameters on GW morphology are separated. By using a concatenated design matrix, feature vectors contain *only* morphology relevant to either A or $\beta_{ic,b}$.

In Table IV, we list results from this encoding. As the strength of differential rotation decreases, the significance decreases (the p -values become larger). These results are more trustworthy than those given in Tab. II, because the effects on the waveforms due to $\beta_{ic,b}$, which are found to be much stronger than those due to differential rotation,

have been factored out.

C. Interactions Between Differential and Total Rotation

Abdikamalov *et al.* [19] find evidence for important inter-dependencies between differential rotation and total rotation. For slowly rotating progenitors leading to $\beta_{ic,b} \lesssim 0.04$ to 0.08, the waveforms are essentially independent of differential rotation. Only at higher values of $\beta_{ic,b}$ is differential rotation influential on the GW signal shape.

In order to examine the dependencies between total and differential rotation, we can encode *two-way interactions* between the differential and total rotation parameters. A two-way interaction means waveforms are grouped by two parameters, allowing their joint effect on waveform morphology to be recovered (see Sec. IID 4 for a detailed explanation). For instance, we may consider waveforms with $\beta_{ic,b} \lesssim 0.05$ and the $A1$ differential rotation as a single group, and then test whether these waveforms have a distinct morphology.

Results from Tables I, II and IV suggest that waveforms with $A3$, $A4$ and $A5$ differential rotation profile can be grouped together, due to the lack of evidence for significant differences between these groups. In order to reflect this new grouping, we alter the differential rotation parameter labeling, using the letter ‘U’ to reflect that these waveforms are from uniformly to moderately differentially rotating progenitors:

- $A1 = A1$, 30 waveforms;
- $A2 = A2$, 22 waveforms;
- $AU = A3, A4$ and $A5$, 40 waveforms.

Our partitioning of the physical parameters into three different differential rotation ranges and three total rotation ranges leads to nine different two-way interactions to test, in addition to six tests of the deviation encoding on A and $\beta_{ic,b}$. The results are given in Table V. We find that all p -values are lower than 0.01, except those for interactions involving the $A2$ waveforms.

Therefore, there is no evidence for a strong inter-dependence of $A2$ waveforms on $\beta_{ic,b}$ — the three features for the $A2$ with βS , βM and βR waveforms are not significant. The changes in the $A2$ waveforms due to $\beta_{ic,b}$ are better explained by the $\beta S - \mu$, $\beta M - \mu$ and $\beta R - \mu$ features. This is not the case for the other differential rotation levels, whose waveforms as a whole exhibit varying, but generally strong degrees of inter-dependence with $\beta_{ic,b}$.

Since rotating core collapse is a highly non-linear process, it is not surprising to find strong inter-dependencies between these two parameters. To highlight the connection of our work to the PC-based methods of Heng [10] and Röver *et al.* [13], we use student’s t statistic to examine the importance of individual principal components

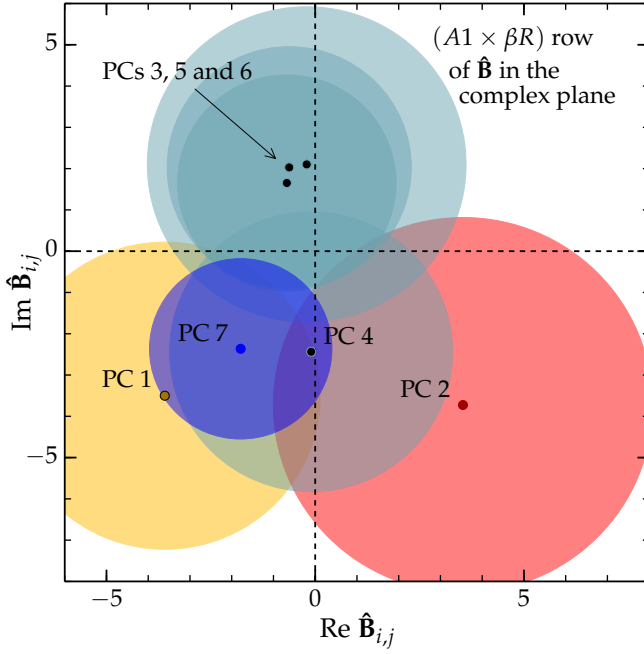


FIG. 5. 95% Confidence circles in the complex plane for the i th row of $\hat{\mathbf{B}}$, which contains the PC coefficients of the $(A1 \times \beta R)$ interaction feature vector. The column of the design matrix $(A1 \times \beta R)$ was encoded into determines the value of i . The $(A1 \times \beta R)$ feature vector describes waveforms that are both highly differentially rotating ($A1$) and have a rapid total rotation (βR). The PC coefficients of row $\hat{\mathbf{B}}_i$ are marked in black. The $j = 3, 4, 5, 6$ PC coefficients overlap the origin and their 95% confidence circles are shaded in subdued colors. From this plot, we can see that the $(A1 \times \beta R)$ feature vector is primarily determined by the $j = 1, 2$ and 7 PCs, whose confidence circles do not overlap zero.

(PCs) in one of the interaction terms. The two-way interaction between $A1$ and βR , labeled $A1 \times \beta R$ in Table V, resulted in the lowest p -value of the interactions tested, 5.6×10^{-15} . Abdikamalov *et al.* [19] also find that the distribution of angular momentum (differential rotation) is most relevant to the GW signal for very rapidly rotating cores (high $\beta_{ic,b}$).

In order to visualize the solutions (rows of $\hat{\mathbf{B}}$) obtained by our regression approach, we plot confidence intervals around the PC coefficients used to reconstruct waveforms in the $A1 \times \beta R$ waveform group in Fig. 5. From Fig. 5, we find that PCs 1, 2, and 7 are primarily responsible for uniquely characterizing the set of waveforms that were generated from strongly differentially rotating progenitors with rapidly rotating cores.

D. Ability of the Model to Reconstruct Waveforms

In this section, we again use a deviation encoding to model the differential rotation parameter, and for $\beta_{ic,b}$, transition to the use of a polynomial encoding. For the time being, we neglect two-way interaction terms

TABLE V. Results of comparisons of two-way interactions between waveforms grouped into three differential rotation (A) categories, and into three ranges of total rotation ($\beta_{ic,b}$). The only set of interactions that are found to be not significant (p -value ≥ 0.01) are those involving waveforms with the $A2$ differential rotation profile. All catalog waveforms were scaled to a distance of 10 kpc. An asterisk (*) marks results that are considered significant (large values of T^2 producing p -values at or below 0.01 are considered “significant”).

Comparison	Hottelling's T^2	p -value
$A1 - \mu$	64.9	$1.4 \times 10^{-13}*$
$A2 - \mu$	21.57	$7.5 \times 10^{-4}*$
$AU - \mu$	39.88	$3.9 \times 10^{-8}*$
$\beta S - \mu$	353.52	0.0*
$\beta M - \mu$	157.53	0.0*
$\beta R - \mu$	561.72	0.0*
$A1 \times \beta S$	36.40	$2.5 \times 10^{-7}*$
$A1 \times \beta M$	36.10	$2.9 \times 10^{-7}*$
$A1 \times \beta R$	71.94	$5.6 \times 10^{-15}*$
$A2 \times \beta S$	6.23	0.64
$A2 \times \beta M$	7.79	0.42
$A2 \times \beta R$	10.72	0.15
$AU \times \beta S$	32.40	$2.2 \times 10^{-6}*$
$AU \times \beta M$	31.63	$3.3 \times 10^{-6}*$
$AU \times \beta R$	44.92	$2.8 \times 10^{-9}*$

between polynomials of $\beta_{ic,b}$ and differential rotation. The polynomial encoding of $\beta_{ic,b}$ is useful for associating trends in GW morphology with changing values of $\beta_{ic,b}$. While results can be more difficult to interpret in an analysis due to the multivariate nature of the waveforms, polynomial terms can still provide insight into waveform morphology.

Encoding the continuous valued $\beta_{ic,b}$ parameter with polynomials also avoids the need to specify bin ranges. For continuous parameters, it is generally difficult to choose the number of bins and the range each bin covers.

Higher order polynomials in the design matrix are also a good way to obtain accurate reconstructions of catalog waveforms. We build a fifth order polynomial model for the $\beta_{ic,b}$ parameter to see how well our model can fit the catalog. If there are n data points on some two dimensional scatter plot, an n th order polynomial is required to exactly fit the data points [14]. This logic applies in the multivariate case as well. With n waveforms, an n th order polynomial can provide a perfect fit. We use a 5th order polynomial of $\beta_{ic,b}$ that is flexible enough to fit shapes similar to those in Fig. 10 of Abdikamalov *et al.*, but also has a low enough order to avoid oscillations between interpolated points associated with high-order polynomials (Runge's phenomenon).

After forming a design matrix \mathbf{X} with a deviation encoding of differential rotation and a polynomial encoding on $\beta_{ic,b}$, we solve for $\hat{\mathbf{B}}$ and use it to reconstruct all catalog waveforms. We then find the set of reconstructed

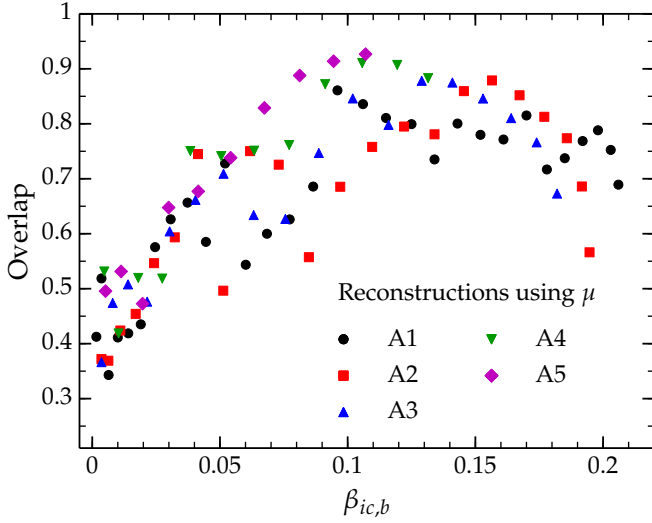


FIG. 6. Overlap as a function of $\beta_{ic,b}$ for the Abdikamalov *et al.* [19] waveforms using only the catalog mean (a design matrix with only a column of ones, denoted μ) to reconstruct the 92 primary waveforms. The differential rotation is represented by various marker types.

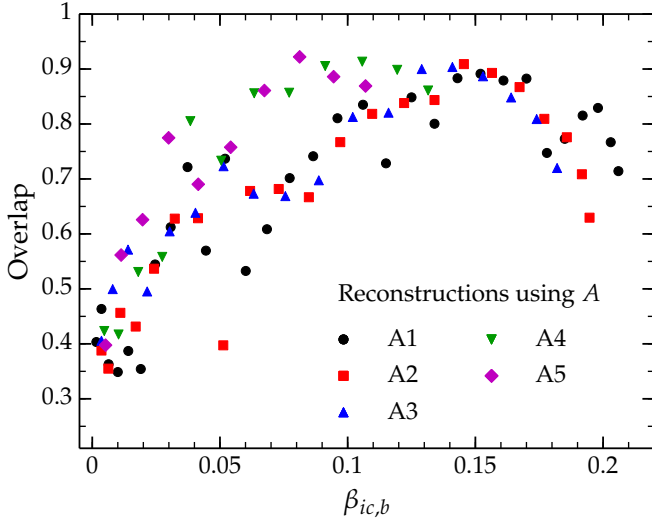


FIG. 7. Overlap as a function of $\beta_{ic,b}$ for the Abdikamalov *et al.* [19] waveforms with a deviation encoding on differential rotation (A) to reconstruct the 92 primary waveforms. Each waveform is reconstructed by the mean waveform and a feature vector associated with a particular differential rotation profile. Slight improvements in overlap from Fig. 6 are noticeable.

waveforms, denoted \mathbf{Y}^R , by simply plugging $\hat{\mathbf{B}}$ into

$$\mathbf{Y}^R = \mathbf{X}\hat{\mathbf{B}}\mathbf{Z}^\dagger, \quad (27)$$

along with the appropriate design matrix \mathbf{X} and PC basis \mathbf{Z}^\dagger .

The criterion we use to determine the accuracy of reconstructions (or predictions) is the detector noise weighted overlap. An overlap of one means two wave-

forms are identical, while an overlap of zero indicates that they are orthogonal. To compute the overlap, we first define the detector noise weighted inner product,

$$\langle g, h \rangle = 2 \int_0^\infty df \frac{\tilde{g}(f)\tilde{h}^*(f) + \tilde{g}^*(f)\tilde{h}(f)}{S_n(f)}, \quad (28)$$

where $\tilde{h}_k(f)$, $\tilde{g}_k(f)$ are the Fourier transforms of $h(t)$ and $g(t)$, two signals we are interested in comparing. The $*$ denotes complex conjugation, and $S_n(f)$ is the known detector noise power spectral density. The overlap, \mathcal{O}_i , of the i th waveform, \mathbf{y}_i with its reconstruction, \mathbf{y}_i^R , is defined as

$$\mathcal{O}_i \equiv \frac{\langle \mathbf{y}_i^R, \mathbf{y}_i \rangle}{\sqrt{\langle \mathbf{y}_i^R, \mathbf{y}_i^R \rangle \langle \mathbf{y}_i, \mathbf{y}_i \rangle}}, \quad (29)$$

which equals one if the two waveforms are entirely in phase, and is zero when they are completely out of phase, where we are keeping the waveforms perfectly aligned throughout.

1. Reconstructions using the catalog mean and differential rotation

We plot four different sets of reconstructions. First, we use only the intercept term μ (the first column of \mathbf{X} in all of our encoding schemes). It can be shown that with only a column of ones in \mathbf{X} , $\mathbf{X}\hat{\mathbf{B}}\mathbf{Z}^\dagger$ is equal to the mean waveform of the catalog, which we denote $\bar{\mathbf{y}}$. This mean waveform (in the time domain) is plotted in black in Fig. 1, and is alternatively found by taking the sum over all columns of \mathbf{Y} and then dividing by the total number of rows,

$$\bar{\mathbf{y}} = \frac{1}{n} \sum_{j=1}^n \mathbf{Y}_j. \quad (30)$$

In this case, $\bar{\mathbf{y}} = \mathbf{y}_i^R$ for all n catalog waveforms. The overlap value for each waveform is plotted as a function of $\beta_{ic,b}$ in Fig. 6. Using $\bar{\mathbf{y}}$ to reconstruct, 48 out of 92 waveforms ($\sim 52\%$) have an overlap greater than or equal to 0.7, indicating that many of the catalog waveforms share a similar general form. We also observe that waveforms with $\beta_{ic,b} \lesssim 0.1$ are much more difficult to reconstruct, most likely because they contain stochastic signal features from convection. To a lesser extent, waveforms from rapidly rotating progenitors, $\beta_{ic,b} \gtrsim 0.15$, are also more unlike $\bar{\mathbf{y}}$. There appears to be no clear and visible indication of a dependence of overlap on differential rotation, whose values are denoted in Fig. 6 by the colored symbols.

Next, in Fig. 7, we solve for $\hat{\mathbf{B}}$ using the intercept (μ) and the four deviation encoded columns for differential rotation. There is a small but noticeable improvement in the reconstruction errors. In this case, 53 waveforms out of 92 have an overlap greater than 0.7 ($\sim 58\%$).

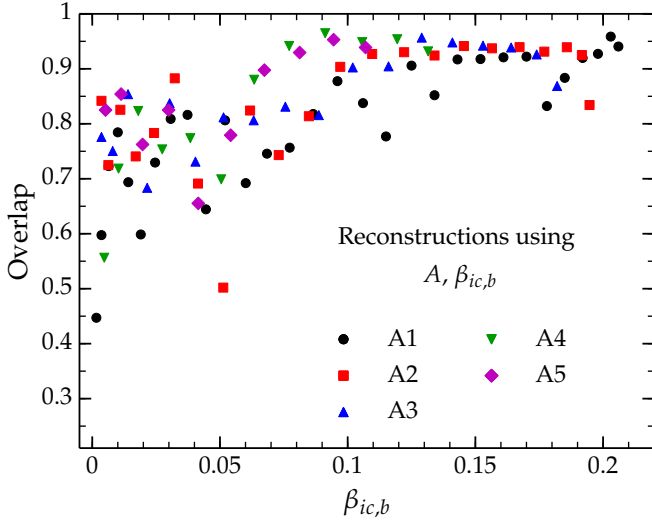


FIG. 8. Overlap as a function of $\beta_{ic,b}$ for the 92 Abdikamalov *et al.* [19] waveforms. A deviation encoding of A , as well as a 5th order polynomial function of $\beta_{ic,b}$, is encoded and fit. Including the $\beta_{ic,b}$ parameter in the design matrix produces a large increase in the overlaps over the encoding used in Fig. 7.

Again, there appears to be more difficulty in reconstructing waveforms from more slowly or more rapidly rotating progenitors, but no obvious dependence on differential rotation.

2. Improving Reconstructions by Incorporating $\beta_{ic,b}$ and Two-way Interactions

We include a 5th order polynomial on $\beta_{ic,b}$ in the design matrix, in addition to a deviation encoding of differential rotation (both encodings necessitate the inclusion of a column of ones (μ) in the design matrix). This encoding provides a dramatic increase in the overlap between the waveforms and their reconstructions, as shown in Fig. 8. The reconstructions are excellent for waveforms with $\beta_{ic,b} \gtrsim 0.1$. In total, 83 of the waveforms now have an overlap greater than or equal to 0.7 ($\sim 90\%$). This improvement corroborates our findings using p -values about the strength of the correlation between GW morphology and total rotation. Interestingly, there is a kink in the overlaps near $\beta_{ic,b} \sim 0.05$, indicating a point in the progenitor parameter space whose waveforms are particularly difficult to reconstruct. We note from Fig. 10 in Abdikamalov *et al.* that when $\beta_{ic,b} \approx 0.05$, the amplitude of the waveforms' largest peak (the bounce peak, denoted $h_{1,neg}$) begins to change as A varies. Both of our results indicate that $\beta_{ic,b} \approx 0.05$ is a particularly volatile point in the parameter space of rotating core collapse.

While including a polynomial encoding of $\beta_{ic,b}$ improves the overlap, waveforms from slowly rotating progenitors are still less accurately reconstructed. This is suggestive of two things. First, slowly spinning mod-

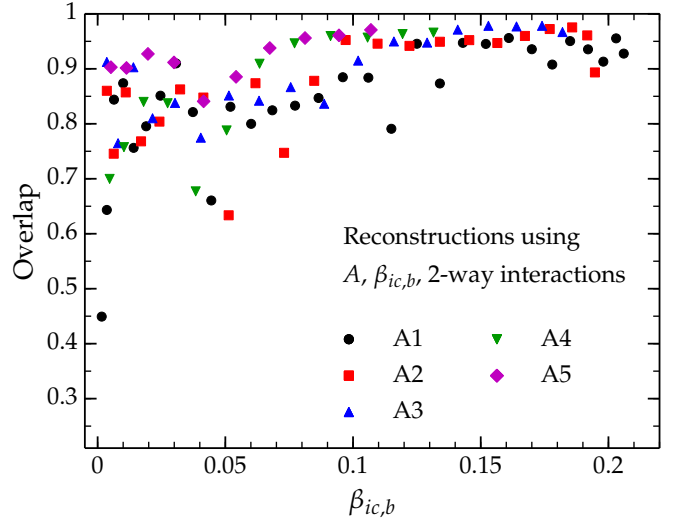


FIG. 9. Overlap as a function of $\beta_{ic,b}$ for the 92 Abdikamalov *et al.* waveforms. This time, we use a deviation encoding of A , a 5th order polynomial function of the $\beta_{ic,b}$, as well as interactions between each of the 5 polynomial terms and the A parameter. This encoding produces the most accurate reconstructions of the catalog waveforms for the encodings we examine.

els emit GW signals with stronger stochastic effects due to prompt postbounce convection [19, 42]. This effect is problematic for our statistical analysis due to the form of the Hotelling's T^2 and student's t test statistics. Both of these statistics are weighted by the residual covariance matrix, Σ_R , which is solved for using the entire waveform catalog. This procedure implicitly assumes that the residuals of waveforms comprising the entire parameter space have the same covariance structure. We leave a detailed analysis of the covariance structure of the residuals for further work. Second, a 5th order polynomial model may provide an inadequate description for waveforms from slowly rotating progenitors. A higher-order polynomial, or a different type of basis function may be required to accurately capture the variation in the waveforms from more slowly rotating progenitors.

Next, we build a design matrix that includes interactions between A and $\beta_{ic,b}$. This design matrix has one column in \mathbf{X} for μ , four columns for a deviation encoding of A , five columns for the 5th order polynomial function of $\beta_{ic,b}$, and 20 interaction columns between each term in the $\beta_{ic,b}$ encoding and each term in the A encoding. Including interactions results in large overlaps for nearly all the waveforms in the Abdikamalov *et al.* [19] waveform catalog. This is shown in Fig. 9. Of the 92 primary waveforms, 88 have an overlap greater than or equal to 0.7 ($\sim 96\%$). Most of the waveforms ($\sim 57\%$) even have an overlap $\gtrsim 0.9$. Again, most of these are from moderate to rapid rotators with $\beta_{ic,b} \gtrsim 0.06 - 0.08$. We also note that the kink at $\beta_{ic,b} \sim 0.05$ in Fig. 9 has become somewhat more pronounced.

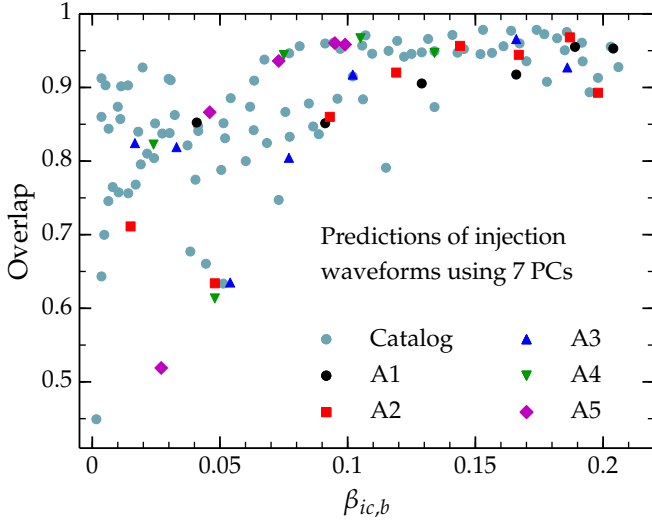


FIG. 10. Predictions of the 31 Abdikamalov *et al.* injection waveforms (see Sec. II A) using the design matrix used to produce Fig. 9. For comparison, we include the catalog reconstructions from Fig. 9 marked as grey dots, denoted “catalog” in the legend. We find that this particular model can predict injections waveforms very well, despite a few outliers.

E. Predicting Injection Waveforms

There is always the chance that our statistical model will be unable to generalize to waveforms with parameterizations not specifically encoded in the design matrix. Alongside their primary catalog of 92 waveforms, Abdikamalov *et al.* [19] also produced a set of 43 waveforms to be used as *injections*. They were used to test the ability of matched filtering and Bayesian model selection methods to measure the physical parameters of GWs injected into simulated detector noise.

To evaluate the ability of our regression model to predict waveforms, we take the subset of 31 injection waveforms that does not include waveforms computed with equations of state and electron capture prescriptions that differ from those of the original catalog. We do this to simplify our analysis and will address dependence on equation of state and electron capture microphysics in future work.

To predict the subset of 31 injection waveforms, we employ our previously fitted regression model whose design matrix was comprised of a deviation encoding of A , a 5th order polynomial model on $\beta_{ic,b}$, and two-way interactions between A and $\beta_{ic,b}$. We use Eq. 17 to rapidly generate these waveforms, given a vector, $\tilde{\mathbf{x}}$, of their properly encoded physical parameters.

In Fig. 10, we plot the overlap of the injections and their predictions. For comparison, we show in light grey dots the overlaps of the reconstructed waveforms of the original waveform set. These are copies of the markers shown in Fig. 9. The colored markers show the overlap as a function of $\beta_{ic,b}$ of the 31 injection waveforms with

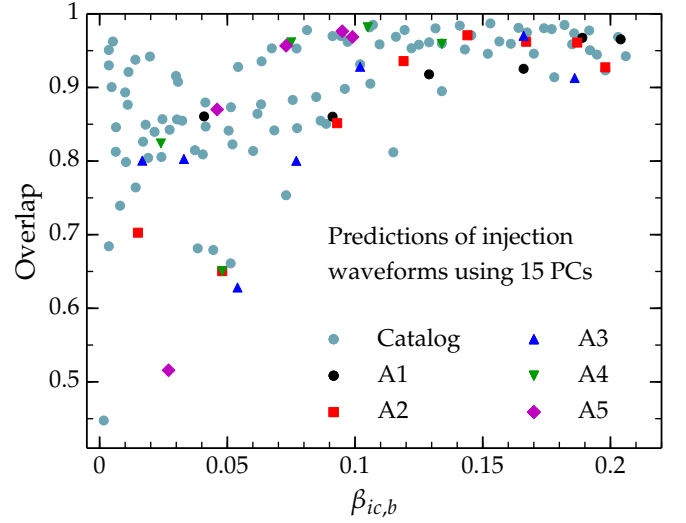


FIG. 11. Predictions of the 31 Abdikamalov *et al.* injection waveforms (see Sec. II A) using the design matrix used to produce Fig. 9. This plot was created identically to Fig. 10, except 15 instead of 7 PCs were used to reconstruct the 91 catalog waveforms (gray dots) and predict the injection waveforms. We find that using a larger number of PCs has little change on the reconstruction and prediction overlaps.

their predictions. Many of the injection waveforms are predicted as well as the waveforms in the original set are reconstructed. The presence of a few outliers (mostly at small to moderate $\beta_{ic,b}$) indicates that there is room to improve our encodings of the physical parameters.

Next, we reproduce Fig. 10 using 15 instead of 7 PCs in the regression model. Fig. 11 shows that increasing the number of PCs in our basis from 7 to 15 achieves only a marginal increase in overlap for both the original and the injection waveform sets. This indicates that the first several PCs capture the large majority of physically significant waveform content. While there is currently no clear rule that could guide us in choosing the appropriate number k of PCs to use, we find that in this context the choice of k (as long as it is “large enough”) has a small impact on results.

We also test if the predicted waveform for the parameters associated with a given injection waveform actually has its greatest overlap with that waveform and not with some other waveform of the injection set. In the top panel of Fig. 12, we mark the actual injection waveform nearest to its prediction. We do this as a function of the dominant parameter $\beta_{ic,b}$. If an injection has the highest overlap with its prediction, then it is marked on the diagonal dashed line. We find that most of these marks lie on, or close to, the diagonal. Hence, in most cases the predicted waveform is identified with the injection waveform whose parameters were used for its prediction.

In the top panel of Fig. 12, at $\beta_{ic,b} \approx 0.05$, four of the predictions are considerably nearer to the $\beta_{ic,b} \approx 0.07$ injection waveforms. Otherwise, only two other injections have sub-optimal predictions, the A2, $\beta_{ic,b} = 0.093$ and

the A3, $\beta_{ic,b} = 0.186$ injection waveforms. We also note from the top panel of Fig. 12 that the prediction for the A5, $\beta_{ic,b} = 0.027$ injection waveform is very near the diagonal, despite the fact that it has the lowest overlap with its reconstruction in Figs. 10 and 11. Thus, its overlap with other injection waveforms must be even lower.

In the bottom panel of Fig. 12, we plot the $\beta_{ic,b}$ of the predicted injection waveform versus the difference in A between the predicted injection waveform and the nearest injection waveform. We note that for each instance where the difference in A is not equal to zero, the same waveform in the top panel is marked off the diagonal. Since there are only 31 injection waveforms, a lack of overlap between the prediction and the injection due to a problem fitting $\beta_{ic,b}$ results in A being predicted incorrectly, because $\beta_{ic,b}$ is the dominant parameter. In further work we plan on exploring different approaches to modeling the waveforms' dependence on $\beta_{ic,b}$.

Figures 10, 11, and 12 taken together show that our regression approach produces good predictions for $\beta_{ic,b} \gtrsim 0.06$ waveforms. Potentially, waveform dependence on rotation below $\beta_{ic,b} \approx 0.06$ is inadequately fitted by a 5th order polynomial. In addition, the appearance of post-bounce prompt convection at slow to moderate rotation and the associated appearance of stochastic GW signal features may spoil our analysis.

IV. SUMMARY AND FURTHER WORK

In this work, we have described a multivariate regression approach for the analysis of simulated gravitational waveforms from rotating core collapse. The solutions of our regression model are *feature vectors* — pieces of waveform morphology *directly* attributable to encoded physical parameters. While specific values of discrete physical parameters are encoded individually, we have also considered continuous parameter encodings to describe linear and non-linear waveform dependence.

By constructing feature vectors from linear combinations of principal components (PCs), we provided a means to connect the PC based methods of previous work [10, 13, 16] to the physical parameters underlying rotating core collapse. Within the regression framework, we use statistical hypothesis testing to quantitatively measure how strongly feature vectors (thus physical parameters) influence waveform morphology in the presence of Gaussian noise of a single gravitational-wave detector.

Finally, we used our regression model to *reconstruct* and *predict* GWs from a given PC basis and set of encoded physical progenitor parameters. These reconstructions and predictions are linear combinations of feature vectors, providing readily interpretable solutions. Our proof-of-principle study showed that our regression scheme reliably interpolates between waveforms from progenitors that have $\beta_{ic,b} \gtrsim 0.06$ (where $\beta_{ic,b}$ is the ratio of rotational kinetic energy to gravitational energy of the

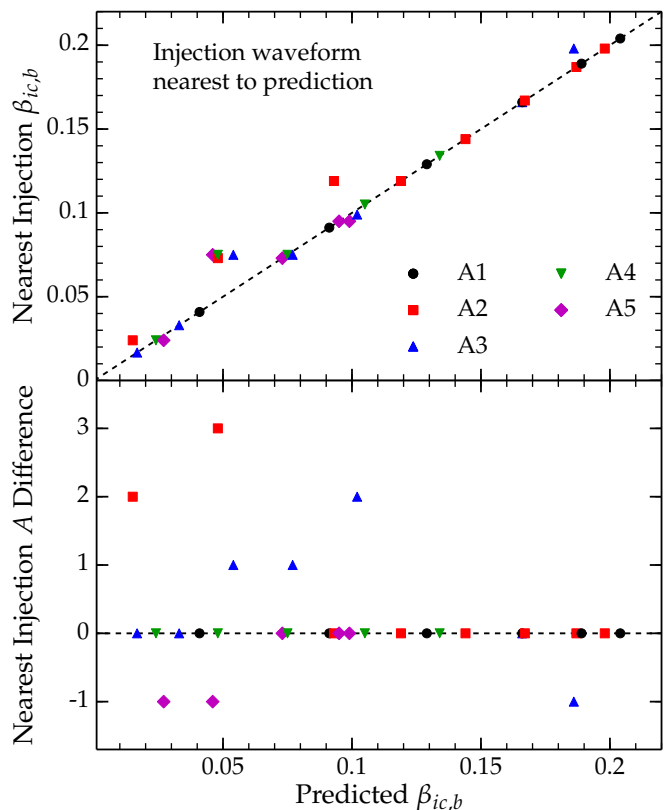


FIG. 12. After predicting the 31 waveforms in the injection set, we mark the injection waveform that has the highest overlap with the predicted waveform. If the i th mark lies on the dotted black line, then the prediction of the i th injection waveform has the highest overlap with the i th injection waveform. In the top panel, we plot the $\beta_{ic,b}$ of the nearest injection waveform versus the $\beta_{ic,b}$ value of the predicted waveform. In the bottom panel, we plot the difference in A between the predicted waveform and the nearest injection waveform as a function of $\beta_{ic,b}$.

inner core at bounce).

We demonstrated our methodology on the recent Abdikamalov *et al.* [19] rotating core collapse waveform catalog. Their core-collapse models are determined by two rotation parameters, differential rotation (A) and $\beta_{ic,b}$. Our statistical hypothesis test based study of waveform parameter dependence corroborates the more qualitative analysis within [19]. The axisymmetric simulations of Abdikamalov *et al.* [19] produced linearly polarized gravitational waveforms. As full 3D models of stellar collapse and postbounce supernova evolution mature, we will need to adapt our regression scheme to handle waveforms with multiple polarizations and consider noise in gravitational-wave detector networks.

While we have shown that our regression strategy is effective for rotating core collapse waveforms, it remains to test its ability on other gravitational-wave emission processes in stellar collapse and core-collapse supernovae. For example, in the context of neutrino-driven explosions in nonrotating or slowly rotating progenitors, convective

motions introduce stochastic components into the produced gravitational waves. While able to extract deterministic waveform features, our current regression model cannot handle stochastic waveform components or varying degrees of stochasticity dependent on progenitor parameters.

The primary focus of this work was on analyzing the relationships between physical parameters and generated waveforms. In the future, we intend to shift our focus to waveform prediction in the context of parameter estimation for observed signals. With the rich statistical literature on regression modeling, there are many avenues to explore. We found that our waveform predictions using 5th order polynomials of $\beta_{ic,b}$ are not as accurate for slowly and moderately rapidly rotating stellar cores with $\beta_{ic,b} \lesssim 0.06$. Possibly, the degree of stochasticity increases within cores at lower values of $\beta_{ic,b}$. Also, polynomials may not be the most effective basis for expressing waveforms' dependence on $\beta_{ic,b}$. Other bases, such as splines or radial basis functions [14] may provide better fits. Additionally, Gaussian Process regression methods [43] do not require one to specify a specific basis for continuous physical parameters, and have been shown to capably fit trends of arbitrary complexity.

Multi-dimensional stellar collapse and core-collapse supernova simulations are still computationally challenging and time consuming. This currently prohibits the construction of dense waveform catalogs exploring the full

range of the physical parameter space. The ability to confidently predict waveforms given an arbitrary set of parameter values (and a set of physical parameters and waveforms that can be spanned by a PC basis) enables template-bank based parameter estimation methods for linearly polarized gravitational waves from rotating core collapse. In future work, this capability must be extended to include other important emission mechanisms, such as neutrino-driven convection, asymmetric neutrino emission, and nonaxisymmetric rotational instabilities.

ACKNOWLEDGMENTS

We acknowledge helpful discussions with and help from members of the LIGO Scientific Collaboration and Virgo Collaboration Supernova Working Group, in particular Sarah Gossan, I. Siong Heng, and Nelson Christensen. BE and RF are supported in part by NSF grant PHY-1205952. CDO is partially supported by NSF CAREER grant PHY-1151197, NSF gravitational physics grant PHY-0904015, The Sherman Fairchild Foundation, and the Alfred P. Sloan Foundation. Some of the computation performed towards the results presented here used NSF XSEDE computing resources under award TG-PHY100033.

-
- [1] C. D. Ott, *Class. Quantum Grav.* **26**, 063001 (2009).
 - [2] H. A. Bethe, *Rev. Mod. Phys.* **62**, 801 (1990).
 - [3] H.-T. Janka, F. Hanke, L. Hüpfol, A. Marek, B. Müller, and M. Obergaulinger, *Prog. Th. Exp. Phys.* **2012**, 01A309 (2012).
 - [4] G. M. Harry and the LIGO Scientific Collaboration, *Class. Quantum Grav.* **27**, 084006 (2010).
 - [5] The Virgo Collaboration, *Tech. Rep. VIR-0027A-09* (2009), URL <https://tds.ego-gw.it/itf/tds/file.php?callFile=VIR-0027A-09.pdf>.
 - [6] S. M. Adams, C. S. Kochanek, J. F. Beacom, M. R. Vagins, and K. Z. Stanek, *Astrophys. J.* **778**, 164 (2013).
 - [7] K. Kotake, *Comptes Rendus Physique* **14**, 318 (2013).
 - [8] P. R. Brady and S. Ray-Majumder, *Class. Quantum Grav.* **21**, S1839 (2004).
 - [9] T. Zwerger and E. Müller, *Astron. Astrophys.* **320**, 209 (1997).
 - [10] I. S. Heng, *Class. Quantum Grav.* **26**, 105005 (2009).
 - [11] T. Summerscales, A. Burrows, L. S. Finn, and C. D. Ott, *Astrophys. J.* **678**, 1142 (2008).
 - [12] C. D. Ott, A. Burrows, E. Livne, and R. Walder, *Astrophys. J.* **600**, 834 (2004).
 - [13] C. Rover, M. A. Bizouard, N. Christensen, H. Dimmelfeier, I. S. Heng, and R. Meyer, *Phys. Rev. D* **80**, 102004 (2009).
 - [14] R. Tibshirani and J. Friedman, *The Elements of Statistical Learning: Data Mining, Inference, and Prediction* (Springer-Verlag, New York, 2001).
 - [15] C. D. Ott, *Class. Quantum Grav.* **26**, 204015 (2009).
 - [16] J. Logue, C. D. Ott, I. S. Heng, P. Kalmus, and J. H. C. Scargill, *Phys. Rev. D* **86**, 044023 (2012).
 - [17] R. F. Potthoff and S. N. Roy, *Biometrika* **51**, 313 (1964).
 - [18] G. O. Zerbe and R. H. Jones, *J. Amer. Statist. Assoc.* **75**, 507 (1980).
 - [19] E. Abdikamalov, S. Gossan, A. M. Demaio, and C. D. Ott, Submitted to *Phys. Rev. D*, arXiv:1311.3678 (2013).
 - [20] G. S. Bisnovatyi-Kogan, *Astron. Zh.* **47**, 813 (1970).
 - [21] A. Burrows, L. Dessart, E. Livne, C. D. Ott, and J. Murphy, *Astrophys. J.* **664**, 416 (2007).
 - [22] S. A. Balbus and J. F. Hawley, *Astrophys. J.* **376**, 214 (1991).
 - [23] T. Takiwaki and K. Kotake, *Astrophys. J.* **743**, 30 (2011).
 - [24] P. Mösta, S. Richers, C. D. Ott, R. Haas, A. L. Piro, K. Boydstun, E. Abdikamalov, C. Reisswig, and E. Schnetter, *Astrophys. J.* **785**, L29 (2014).
 - [25] C. D. Ott, H. Dimmelfeier, A. Marek, H.-T. Janka, I. Hawke, B. Zink, and E. Schnetter, *Phys. Rev. Lett.* **98**, 261101 (2007).
 - [26] S. Scheidegger, S. C. Whitehouse, R. Käppeli, and M. Liebig, *Class. Quantum Grav.* **27**, 114101 (2010).
 - [27] C. D. Ott, E. Abdikamalov, E. O'Connor, C. Reisswig, R. Haas, P. Kalmus, S. Drasco, A. Burrows, and E. Schnetter, *Phys. Rev. D* **86**, 024026 (2012).
 - [28] G. Strang, *Introduction to Linear Algebra* (Wellesley Cambridge Press, Wellesley, MA, 1993).
 - [29] D. Shoemaker, *Tech. Rep. LIGO-T0900288-v3*, LIGO Scientific Collaboration (2010), URL

- <https://dcc.ligo.org/cgi-bin/DocDB/ShowDocument?docid=t0900288>.
- [30] D. Brillinger, *Time Series: Data Analysis and Theory* (McGraw-Hill, New York, 1981).
 - [31] J. I. Marden, *Multivariate Statistics : Old School* (2011), URL <http://istics.net/pdfs/multivariate.pdf>.
 - [32] N. C. Giri, *Multivariate Statistical Inference* (Academic Press, Inc., New York, 1977).
 - [33] J. Veitch and A. Vecchio, Phys. Rev. D **81**, 062003 (2010).
 - [34] L. S. Finn, Phys. Rev. D **46**, 5236 (1992).
 - [35] J. Cohen and P. Cohen, *Applied Multiple Regression/Correlation Analysis for the Behavioral Sciences* (Lawrence Erlbaum Associates, Inc., Mahwah, NJ, 1983).
 - [36] R. C. Serlin and J. R. Levin, J. Educ. Stat. **10**, 223 (1985).
 - [37] K. Cannon, C. Hanna, and D. Keppel, Phys. Rev. D **84**, 5 (2011).
 - [38] J. Beringer et al. (Particle Data Group), Phys. Rev. D. **86**, 010001 (2012).
 - [39] H. Hotelling, Ann. Math. Stat. **2**, 360378 (1931).
 - [40] J. Frederick, *Statistical Methods in Experimental Physics* (World Scientific Publishing Company, Singapore, 2006).
 - [41] H. Akaike, Ann. I. Stat. Math. **17**, 185 (1965).
 - [42] H. Dimmelmeier, C. D. Ott, and A. Marek, Phys. Rev. D **78**, 064056 (2008).
 - [43] C. Rasmussen and C. Williams, *Gaussian Processes for Machine Learning* (MIT Press, Cambridge, MA, 2006).